

Environmental variation compensated damage classification and localization in ultrasonic guided wave SHM using self-learned features and Gaussian mixture models

Shruti Sawant,¹ Sheetal Patil,¹ Jeslin Thalapil,¹ Sauvik Banerjee,^{2,*} and Siddharth Tallur^{1,†}

¹*Department of Electrical Engineering, Indian Institute of Technology Bombay, Mumbai 400076, MH India*

²*Department of Civil Engineering, Indian Institute of Technology Bombay, Mumbai 400076, MH India*

(Dated: November 12, 2021)

Conventional damage localization algorithms used in ultrasonic guided wave-based structural health monitoring (GW-SHM) rely on physics-defined features of GW signals. In addition to requiring domain knowledge of the interaction of various GW modes with various types of damages, they also suffer from errors due to variations in environmental and operating conditions (EOCs) in practical use cases. While several machine learning tools have been reported for EOC compensation, they need to be custom-designed for each combination of damage and structure due to their dependence on physics-defined feature extraction. Research on the use of deep learning tools such as convolutional neural networks (CNNs) for automated feature extraction in GW-SHM is in a nascent stage and has vast untapped potential for increasing the robustness of GW-SHM systems. In this work, we propose a CNN-based automated feature extraction framework coupled with Gaussian mixture model (GMM) based EOC compensation and damage classification and localization method. Features learnt by the CNNs are used for damage classification and localization of damage by modeling the probability distribution of the features using GMMs. The Kullback-Leibler (KL) divergence of these GMMs with respect to corresponding baseline GMMs are used as signal difference coefficients (SDCs) to compute damage indices (DIs) along various GW sensor paths, and thus for damage localization. The efficacy of the proposed method is demonstrated using FE generated GW-data for an aluminum plate with a network of six lead zirconate titanate (PZT) sensors, for three different types of damages (rivet hole, added mass, notch) at various temperatures (from 0 °C to 100 °C), with added white noise and pink noise to incorporate errors due to EOCs. We also present experimental validation of the method through characterization of notch damage in an aluminum panel under varying and non-uniform temperature profiles, using a portable custom-designed field programmable gate array (FPGA) based signal transduction and data acquisition system. We demonstrate that the method outperforms conventional EOC compensation method using GMM with physics-defined features for damage localization in GW-SHM systems prone to EOC variations.

Keywords: Convolutional neural networks (CNN), structural health monitoring (SHM), ultrasonic non-destructive testing (NDT), Gaussian mixture model (GMM), damage localization

I. INTRODUCTION

Structural health monitoring (SHM) systems employed for detecting defects in large infrastructure such as bridges, aircraft, railway tracks etc. consist of large number of sensors mounted on the structure to perform a variety of measurements to satisfy the vastly different requirements across different structures and applications. Ultrasonic guided wave-based SHM (GW-SHM) is popular approach for a variety of structures due to low cost of instrumentation, sensitivity of high frequency waves to small defects, ability of guided waves (GWs) to travel long distances on the structure without attenuation etc.[1–3] However, a significant practical limitation of damage detection algorithms in GW-SHM systems designed in laboratory environment, is susceptibility to errors introduced through variations in environmental and operational conditions (EOCs) such as temperature, moisture absorption, loading etc.[4–9] GW-based damage characterization requires interpreting damage features of

time-series corresponding to GW signals recorded by sensor. Variation in EOCs, including temperature, vibration, loading, moisture etc. result in change in phase and amplitude of GW signals [10, 11]. Identifying effective damage features is crucial to the success of damage characterization. Selection of suitable features usually requires professional knowledge and varies for different structures and types of damages. To relieve the burden of damage feature selection, researchers have been investigating deep learning algorithms to automate damage identification without explicit feature definition in advance. There are number of studies reporting temperature compensation techniques [12, 13]. These can be broadly classified into two classes: baseline signal stretch (BSS) and optimal baseline selection (OBS). In BSS, a single baseline signal (e.g. recorded under nominal operating conditions at room temperature) is stretched to match the signal obtained at different temperatures. In OBS approach, baseline signals are recorded at different temperatures and subsequent computations utilize selection of a baseline signal within the database which is most similar to the monitoring signal recorded during inspection. Other preprocessing techniques to remove the effect of EOC variation recently reported in literature

* sauvik@civil.iitb.ac.in

† stallur@ee.iitb.ac.in

include homoscedastic nonlinear cointegration [14], normalized smoothed envelope threshold (NSET) coupled with high pass filtering [15], variational mode decomposition (VMD) algorithm for denoising and removing seasonal patterns in guided wave signals [16] and cointegration analysis [17, 18].

Machine learning (ML) tools prove useful in modeling complex nonlinear phenomena particularly in the presence of uncertainty. In OBS approach, data-driven techniques are used, wherein training of a model is performed using data collected from prior experiments. In the absence of physical models, these non-parametric methods are useful for successful damage characterization. Data-driven techniques useful for such problems include principal component analysis (PCA) [19], singular value decomposition (SVD) [20] and independent component analysis (ICA) [21]. Among OBS techniques, data driven probabilistic approaches are found to be most effective [22]. Abdeljaber et al. used convolutional neural network (CNN) for vibration-based structural damage detection and localization [23]. Khan et al. demonstrated CNN classifier for analyzing delaminations in composite structures wherein CNNs are trained with 2-dimensional spectrograms obtained from time domain vibration signal using Short Time Fourier Transform [24]. Bao et al. trained deep neural network using gray scale images obtained using time-series vibration signals [25]. CNNs were trained using stacked autoencoders and greedy layer-wise training. To demonstrate the applicability of this architecture, data from a long-span cable-stayed bridge in China was used. In another work, Aria et al. applied deep learning to predict damage size and remaining life of the structure using acoustic emission measurements [26]. Giannakeas et al. demonstrated a method to capture impact of EOC variation on Lamb waves in composites through the Bayesian calibration of a finite element (FE) model using experimental observations and compute the model assisted probability of detection (MAPOD) [27].

While deep learning based algorithms for automated feature extraction have been reported in vibration based SHM system, there are limited reports for GW-SHM. Xu et al. extracted features from GW signals and these features were processed by a CNN designed and trained to further extract high-level features and implement feature fusion for crack evaluation [28]. Pandey et al. have demonstrated a local interpretable model-agnostic explanations (LIME) tool for 1D CNN model to study damages (simulated as well as experimental) in aluminum plates [29]. Rautela et al. recently presented extensive performance evaluation of several deep learning approaches assisted with reduced-order spectral finite element models for damage characterization [30]. Ren et al. proposed Gaussian Mixture Model (GMM) based model for compensation of time varying temperature [31–33]. This involves direct extraction of features using time-domain signal recordings, without performing additional transforms. Another example of OBS method for non-uniform temperature gradient on experimental data acquired us-

ing sensor array placed on aluminum plate was presented by Sun et al. [34]. Wang et al. explored the effect of such coupling of two EOC parameters, namely loading and temperature, on GW characteristics [35]. They utilized compensation strategy based on matching pursuit algorithm wherein features calculated using amplitude and group velocity are used for training the model. Khurjekar et al. have reported deep learning models for feature extraction and damage localization in GW-SHM system wherein the variations in environmental factors are modeled as uncertainties in the data [36], albeit without any estimate of damage intensity. Liu et al. used convolutional neural network based framework to represent damage characterization problem as image classification problem [37]. There have been limited reports of using deep learning approaches for damage characterization, albeit in absence of variation in EOCs [37, 38]. It emerges that research on application of deep neural networks for EOC compensation has been limited and has extensive scope for performance evaluation and optimization.

Conventional algorithms for damage localization use manually computed features based on time and/or frequency domain representation of the signals, and physics-based analysis of impact of damage and EOCs on signal properties (e.g. amplitude, phase, frequency etc.) of GW modes. In this work, we propose a novel method for temperature compensated damage classification and localization using ultrasonic GWs. The method utilizes CNNs to learn the features of GW signals acquired on healthy and damaged structures, and to classify the type of damage. The self-learned features are then analyzed using GMMs for EOC compensation. The GMMs obtained using monitoring data are compared against those obtained with baseline data and the Kullback-Leibler (KL) divergence values of the GMMs are used as signal difference coefficient (SDC) for damage index assessment and damage localization. The utility of this method is validated using GW data from a network of six lead zirconate titanate (PZT) sensors on an aluminum plate at various temperatures (from 0 °C to 100 °C) generated using FE simulations, with added white and pink noise of various signal to noise ratios (SNR: 2 dB, 4.5 dB and 10 dB) and three types of damage (rivet hole, added mass and notch). Typically GW-SHM systems are designed for SNR of the order of 20-50 dB [39]. To maintain such high SNR, large values of actuation voltage are used for the transducers. We demonstrate that the proposed method works efficiently even for much lower values of SNR. Finally, we present experimental validation of this technique for notch damage in an aluminum panel using a custom-designed field programmable gate array (FPGA) based signal transduction and data acquisition system, and demonstrate that the method presented in this work outperforms conventional damage localization algorithms in presence of non-uniform and varying temperature conditions. The stochastic variation in the performance of the algorithm due to added noise is significantly reduced by employing the proposed method as compared to ear-

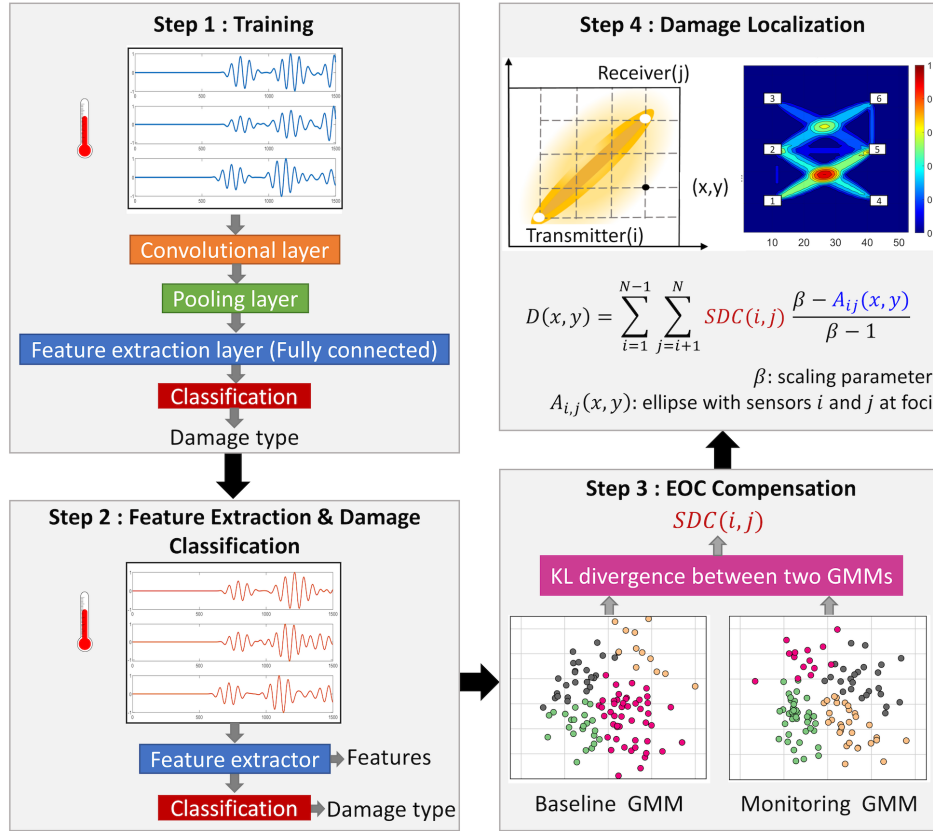


FIG. 1. Illustration of the proposed method using 1D-CNNs for feature extraction and GMMs for temperature compensated damage localization in GW-SHM systems.

lier reported approach for temperature compensation using manually computed features and GMM [31, 32]. For damage localization, features are extracted in automated fashion, without specifying any statistical relation or domain knowledge such as group velocity, choice of wave mode etc. The method presented here thus holds great promise approach for damage localization and characterization in GW-SHM systems prone to EOC variations.

II. CNN+GMM BASED TEMPERATURE COMPENSATED DAMAGE LOCALIZATION METHOD

The proposed method mainly consists of four steps as illustrated in Figure 1:

- **Training:** Instead of manually computing features from time-domain signals, we employ a 1-dimensional (1D) CNN for damage classification and feature extraction using time-domain GW signals. GW signals are recorded for various sensor paths, denoted as pair of transmitter i and receiver j . A CNN is set up for each path, and trained using data for baseline (healthy) and damaged conditions.

- **Feature extraction & damage classification:** Once trained, the penultimate layer of the trained CNN is used for automated feature extraction and damage classification. This feature extraction layer is used to extract features from monitoring data obtained from the structure under maintenance. These features are used for damage classification by assigning labels to training data, as well as damage localization as described in the following steps. Note that several recordings are used for each sensor path in the monitoring stage, to emulate data obtained under various EOCs over various times.
- **EOC compensation:** Next, the features computed in the previous step are used to form clusters using GMMs. This step is crucial for compensating the effect of temperature and other uncertainties. The GMM for each path formed in monitoring stage is compared against the corresponding GMM set up with baseline data. The deviation of the monitoring GMM from baseline GMM is quantified using the KL divergence (i.e. relative entropy of the two probability distributions).
- **Damage localization:** KL divergence of each path $i - j$ is used as the corresponding SDC to compute the damage index and perform damage localization

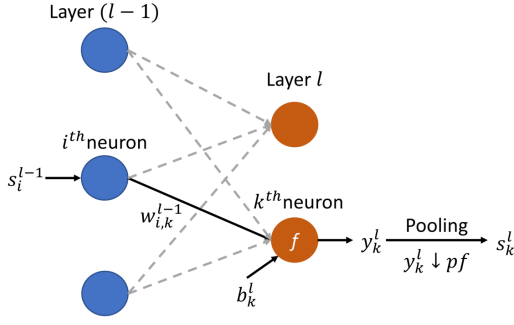


FIG. 2. Illustration of CNN architecture.

using conventional GW SHM damage assessment method [40]. For a sensor network comprising of N sensors, we can obtain $N \times (N - 1)$ SDC values considering all possible sensor pairs, however not all paths may be necessary.

A. CNN based feature extraction

Typical CNN architecture consists of convolutional layers, activation function, pooling layers and a fully connected layer. Convolution operation for 1D time-series data between neuron i of layer $l - 1$ and neuron k of layer l is defined as follows (Figure 2):

$$x_k^l = b_k^l + \sum conv(w_{i,k}^{l-1}, s_i^{l-1}) \quad (1)$$

Here, $conv$ represents the convolution operation, w_{ik} is the weight corresponding to the connection between neuron i of layer $l - 1$ and neuron k of layer l , and b_k^l is the bias of layer l . The result of this convolution operation x_k^l is then processed by a nonlinear activation function f . Typical choices of nonlinear activation functions include rectified linear activation function (ReLU), sigmoid, tanh etc. The intermediate output y_k^l of this activation function is expressed as:

$$y_k^l = f(x_k^l) \quad (2)$$

Next, pooling is performed to reduce dimensionality in order to reduce the number of trainable parameters and computational cost in the network, thereby controlling over-fitting. Popularly used pooling method is *max-pooling* wherein, the highest-valued feature in a specified span is retained while other features in the specified span are discarded. Other pooling methods include average pooling or $L2$ -norm pooling. All neurons in the fully connected layer l have connections to activation function outputs from the preceding layer $l - 1$. The set of features of layer l obtained through these operations is defined as:

$$s_k^l = y_k^l \downarrow pf \quad (3)$$

Here, pf represents down-sampling factor used in the pooling operation. The feature set of the final layer of the CNN is used for classification, using the nonlinear sigmoid function to compute the probabilities of the input belonging to various classes (e.g. healthy, or various types of damage such as rivet hole, added mass, notch etc.) Equations (1)-(3) describe the *forward pass* in CNN training. During back propagation step of training CNNs, a cost function is computed using estimated targets and true targets. The network is then iteratively optimised using stochastic gradient descent to obtain optimal values of weights and biases for given time-series dataset (inputs). The training is deemed complete when the cost function saturates, or reduces below a pre-determined threshold. Once training is completed, these optimised weights and biases are used directly for feature extraction, without having to manually compute features using physics-based methods. The penultimate (fully connected) layer of the trained CNN computes features as defined in equation (3), and is therefore used as the feature extractor layer shown in Figure 1. Suppose an n -dimensional time-series is given as input to the CNN, we obtain an m -dimensional feature vector at the output of the feature extractor layer ($m \ll n$). These features are used as inputs for the next step of the method i.e. clustering using GMM for EOC compensation.

B. GMM based EOC compensation

GMM is soft probabilistic clustering model that describes the membership of sample to a set of clusters using a mixture of Gaussian densities [41]. The probabilistic nature of GMM makes it a suitable choice for compensating uncertainties introduced by variations in EOCs. Unlike hard clustering, this method assigns probabilities to a sample belonging to a finite number of Gaussian distributions with unknown parameters. The optimum number of Gaussian components k is determined using *silhouette criterion*. The silhouette score of the GMM takes into account following two components:

- Mean distance between a sample and all other samples in the same cluster
- Mean distance between a sample and all other samples in neighbouring cluster

The silhouette score varies in the range $[-1, 1]$. A larger value of silhouette score indicates well defined clusters. Suppose for baseline data (GMM with k clusters), the Gaussian components are represented as:

$$p(x) = \sum_{i=1}^{i=k} \pi_i \mathcal{N}(x | \mu_i, \sigma_i) \quad (4)$$

Here, the model parameters μ_i , σ_i and π_i denote the mean, standard deviation and weight of i^{th} Gaussian

component. These parameters are obtained using expectation maximisation (EM) algorithm. The probability distribution function (PDF) $p(x)$ for feature x captures the probabilistic nature of baseline time-series data obtained under various EOCs, and represented by features obtained from the CNN. Similarly, the PDF of monitoring data $q(x)$ is also obtained. After obtaining PDFs for both baseline and monitoring data, we need to quantify their mutual difference using an appropriate statistical relation. This is calculated using KL divergence [42], defined as:

$$KL(p||q) = - \sum_x x * p(x) * \log \left[\frac{q(x)}{p(x)} \right] \quad (5)$$

Intuitively, if the probability of an event x from distribution p is significantly different from that of one from distribution q , then the resulting KL divergence magnitude will be large. In case of SHM application, if the monitoring data deviates substantially from baseline data (due to damage), the resulting KL divergence for that sensor path will be large. Therefore, the KL divergence value is used as SDC for computing damage index (DI) and performing damage localization.

C. Damage localization algorithm

This subsection presents a brief overview of the SDC based DI map computation originally presented by Sikdar et al. [40]. For the arrangement shown in step 4 of Figure 1, (x_i, y_i) and (x_j, y_j) denote Cartesian coordinates of transmitter (i) and receiver (j), respectively. The distance between the transmitter and receiver is denoted as $d_{(i,j)}$. The aluminum panel is represented by a 2-dimensional grid, and at each grid point (x, y) , the pixel value for DI map is computed by scaling the ellipse $A_{i,j}(x, y)$ with focii as the transmitter (i) and receiver (j), and corresponding SDC coefficient $SDC(i, j)$:

$$DI(x, y) = \sum_{i=1}^{N-1} \sum_{j=i+1}^N SDC(i, j) \left[\frac{\beta - A_{i,j}(x, y)}{\beta - 1} \right] \quad (6)$$

where β is an empirically determined scaling parameter independent of velocity of the propagating wave. The elliptical contour shaped spatial distribution function with non-negative values, $A_{i,j}(x, y)$ is defined as:

$$A_{i,j}(x, y) = \begin{cases} P_{(i,j)}(x, y), & P_{(i,j)}(x, y) < \beta \\ \beta, & P_{(i,j)}(x, y) \geq \beta \end{cases} \quad (7)$$

where

$$P_{(i,j)}(x, y) = \frac{\sqrt{(x - x_i)^2 + (y - y_i)^2} + \sqrt{(x - x_j)^2 + (y - y_j)^2}}{d_{(i,j)}} \quad (8)$$

The composite DI map is obtained by overlaying ellipses $A_{i,j}(x, y)$ for various transmitter-receiver ($i - j$) paths. Intersections of paths with damage present inline generate pixels with high intensity in the DI map, and therefore are useful for damage localization. Higher contrast between values of SDCs for damaged paths and undamaged paths yields better localization results in the DI map.

III. GENERATION OF TEMPERATURE-AFFECTED GUIDED WAVE DATASET FOR SIMULATION STUDY

Propagation of Lamb waves in a plate depends on the thickness, density and elastic material properties of the structure. For an isotropic plate of thickness h , the Lamb wave dispersion equations are specified as follows[43]:

- Symmetric (S) mode:

$$\frac{\tanh \frac{\beta h}{2}}{\tanh \frac{\alpha h}{2}} = \frac{4k^2 \alpha \beta}{(k^2 + \beta^2)^2} \quad (9)$$

- Anti-symmetric (A) mode:

$$\frac{\tanh \frac{\beta h}{2}}{\tanh \frac{\alpha h}{2}} = \frac{(k^2 + \beta^2)^2}{4k^2 \alpha \beta} \quad (10)$$

where $\alpha = \sqrt{k^2 - \frac{\omega^2}{V_P^2}}$ and $\beta = \sqrt{k^2 - \frac{\omega^2}{V_S^2}}$, $k = \frac{\omega}{c_p}$ is the wave number, ω is the angular frequency of the propagating wave with a phase velocity c_p . V_P and V_S are the velocities of the pressure (P)-wave and shear (S)-wave respectively, expressed as [43]:

$$V_P = \sqrt{\frac{\lambda + 2\mu}{\rho}} \quad (11)$$

$$V_S = \sqrt{\frac{\mu}{\rho}} \quad (12)$$

The terms λ and μ are Lamé's constants, expressed as:

$$\lambda = \frac{\nu E}{(1 + \nu)(1 - 2\nu)} \quad (13)$$

$$\mu = \frac{E}{2(1 + \nu)} \quad (14)$$

The terms E , ν & ρ denote the Young's modulus of elasticity, Poisson's ratio and density of the material, respectively. The group velocity c_g of the wave modes can be expressed as [43]:

$$c_g = c_p + k \frac{dc_p}{dk} \quad (15)$$

Using equations (9) and (10) and wave number k , the phase velocity c_p and group velocity c_g can be calculated for symmetric and anti-symmetric modes in a plate of a specified material (E, ν and ρ), thickness h at frequency $f = \frac{\omega}{2\pi}$. Figure 3 shows phase velocity and group velocity dispersion curves for a 2 mm thick aluminum 6061-T6 alloy plate at room temperature (20 °C). For our analysis, 150 kHz is chosen as the excitation frequency so that the fundamental symmetric mode ($S0$) and anti-symmetric mode ($A0$) can be easily separated. The variation of material properties of Al 6061-T6 with temperature is shown in Figure 4. The material properties are obtained from COMSOL Multiphysics 5.5 material library. The variation of phase velocity and group velocity with temperature ranging from 0 °C to 100 °C are shown in Figure 5(a) and (b), respectively.

The GW propagation in a 530 mm \times 530 mm \times 2 mm Al 6061-T6 alloy plate with surface mounted 20 mm \times 20 mm \times 0.4 mm PZT-5H transducers was studied using FE simulations performed with COMSOL Multiphysics 5.5, wherein the isotropic aluminum plate and PZT transducers were modeled using *Structural Mechanics Module* coupled with *Piezoelectric Solid Interaction* physics and analyzed using *Time Implicit Study*. The accuracy of FE simulation of wave propagation is primarily determined by the mesh size and time increment used in the simulation [44]. For excitation frequency (f) of 150 kHz, the wavelengths of the $S0$ and $A0$ modes in the Al plate are approximately 36 mm and 17 mm, respectively. Previous research on Lamb wave propagation simulations recommends the largest mesh element size to be smaller than $\frac{1}{6}$ of the mode wavelength [45]. Thus, the largest and smallest mesh sizes in the Al plate are set to 5 mm and 2 mm respectively. Physics controlled *Extra Fine* mesh setting was applied for the surface mounted PZT-5H transducers. The time step was chosen to be 0.1 μ s ($> \frac{1}{60f}$). The transmitter PZT was actuated using a 5-cycle sine pulse shaped by a Hanning window as shown in Figure 6(a) expressed as:

$$V = 0.5 \left(1 - \cos \left(\frac{2\pi ft}{5} \right) \right) \sin(2\pi ft) \quad (16)$$

For validation of the impact of temperature on group velocity of the GW modes obtained from the FE model, a baseline (damage free) Al 6061-T6 alloy plate of dimensions 530 mm \times 530 mm \times 2 mm with two surface mounted PZT-5H transducers as shown in Figure 6(b) was modeled. The 5-cycle sine pulse shaped by a Hanning window was applied at the transmitter PZT (1) and the output signal was recorded at the receiver (2), separated by a distance of 300 mm from the transmitter. *Low reflecting edge* boundary condition was imposed on the four free edges of the plate to avoid reflections of the $S0$ & $A0$ modes from the edges. The total simulation time was set to 150 μ s with a time step of 0.1 μ s. The total number of elements in the FE model were 155 614, with 914 717 degrees of freedom. The computation time for each simulation obtained on a 64-bit Intel® Core™-

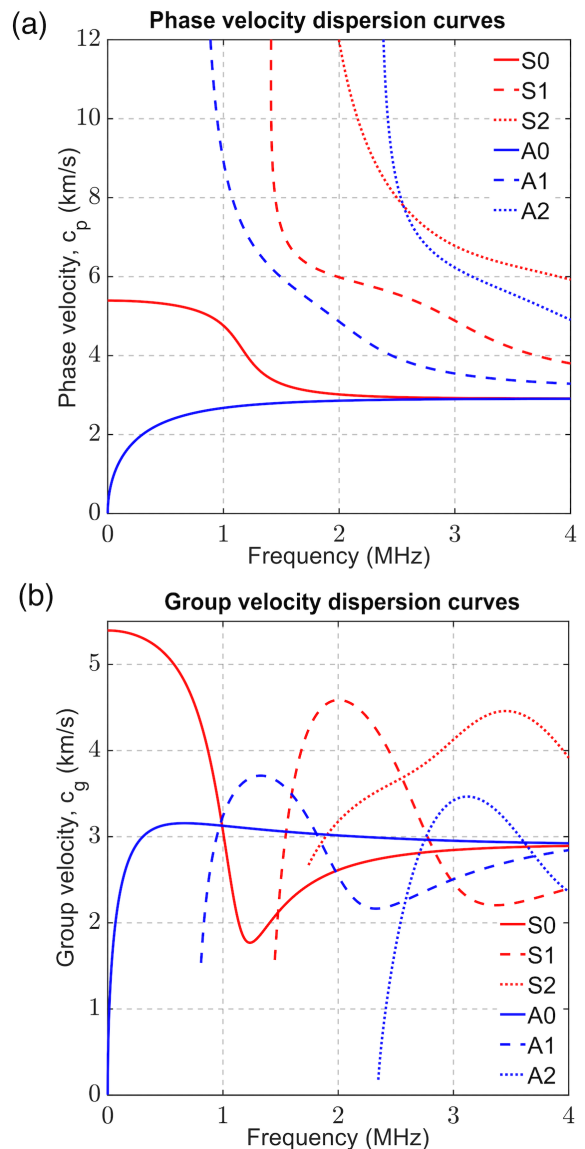


FIG. 3. Dispersion curves of (a) phase velocity, and (b) group velocity for various GW modes in 2 mm thick Al 6061-T6 plate at 20 °C.

i7-7700HQ 2.80 GHz CPU with 16 GB RAM workstation was 5700 s. The *time of flight* for each wave mode was measured using continuous wavelet transform of the output signal measured at the receiver PZT (with Morlet wavelet used as mother wavelet), as shown in Figure 7. Table I shows excellent agreement between the group velocities at 20 °C obtained from FE simulations at to those obtained from analytical calculations (equation (15)).

To evaluate the performance of the damage identification and localization method, FE simulations were carried out on an aluminum 6061-T6 alloy plate of dimensions 530 mm \times 530 mm \times 2 mm with 6 PZT-5H transducers and three types of damages (rivet hole, added mass and notch; parameters listed in Table II) introduced in the lower half of the plate, as shown in Figure 8.

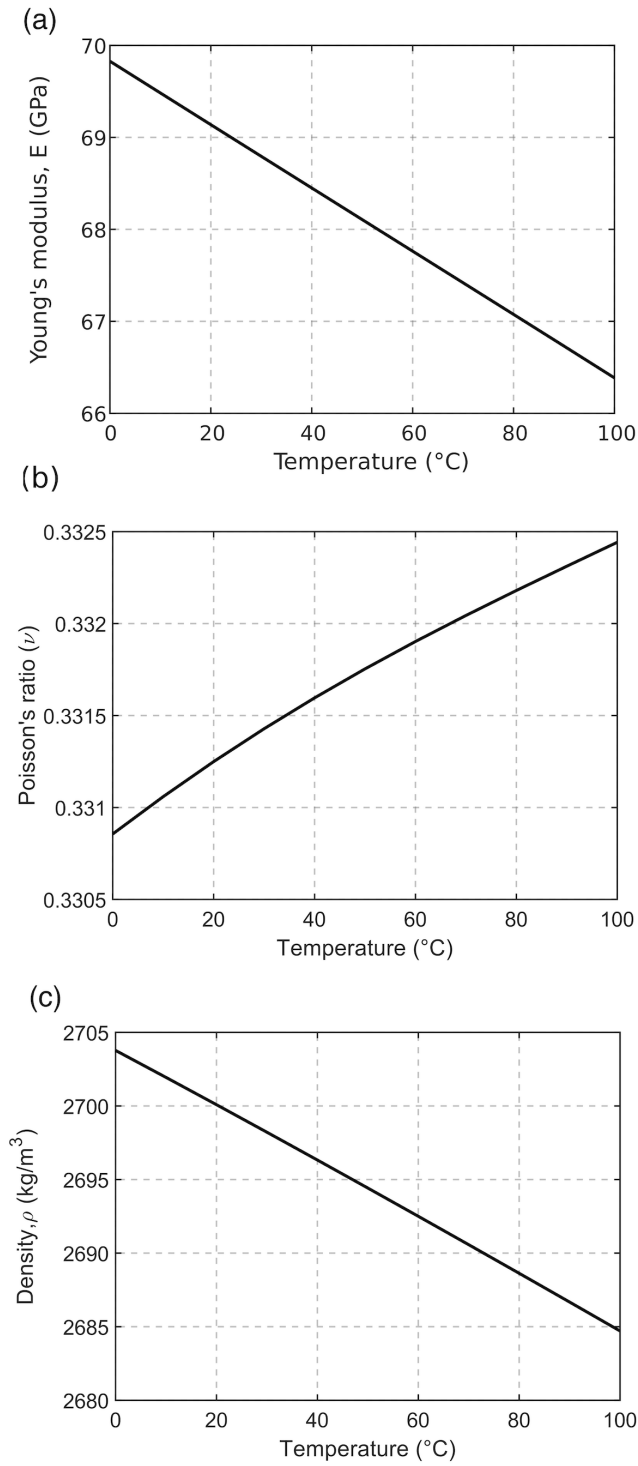


FIG. 4. Variation of (a) Young's modulus, (b) Poisson's ratio, and (c) density of Al 6061-T6 with temperature varying from 0°C to 100°C

Each time-series had a duration of 150 μ s, obtained with a sampling rate of 10 MHz for seven separate transmitter-receiver paths (P12, P15, P24, P25, P26, P53 and P56, where P_{xy} denotes the time-series output obtained with

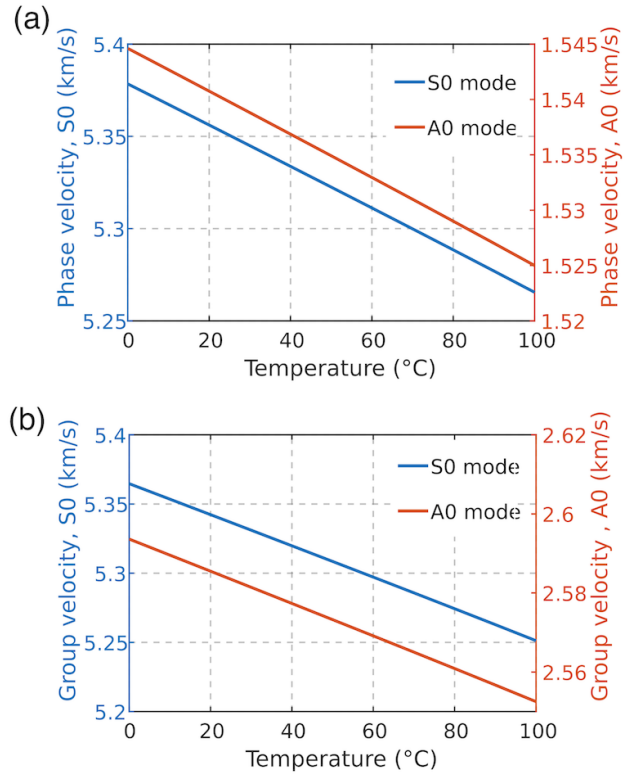


FIG. 5. Variation of (a) phase velocity, and (b) group velocity for S_0 and A_0 modes with temperature varying from 0°C to 100°C.

TABLE I. Comparison of FE measured group velocities with analytically computed values for S_0 and A_0 modes at 20°C

Wave mode	FEM result [km/s]	Analytical [km/s]
S_0	5.128	5.342
A_0	2.671	2.586

TABLE II. Types and parameters of damages studied for evaluation of the proposed damage classification and localization algorithm. The one-hot encoding based class labels used for CNN classification are also listed.

Damage	Parameters	Label
Baseline	-	1000
Rivet hole	Diameter 20 mm	0100
Added mass	Diameter 23 mm, weight 20 g	0010
Notch	60 mm \times 7 mm	0001

PZT x as transmitter and PZT y as receiver). The damage is located at the intersection of the diagonal paths in the lower half of the plate i.e. paths P15 and P24. The FE model had 211 069 elements and 1 210 935 degrees of freedom. The computation time for each simulation (for the mentioned seven paths) obtained on a 64-bit Intel[®] Core[™]-i7-7700HQ 2.80 GHz CPU with 16 GB RAM workstation was 15 290 s. Considering the long time re-

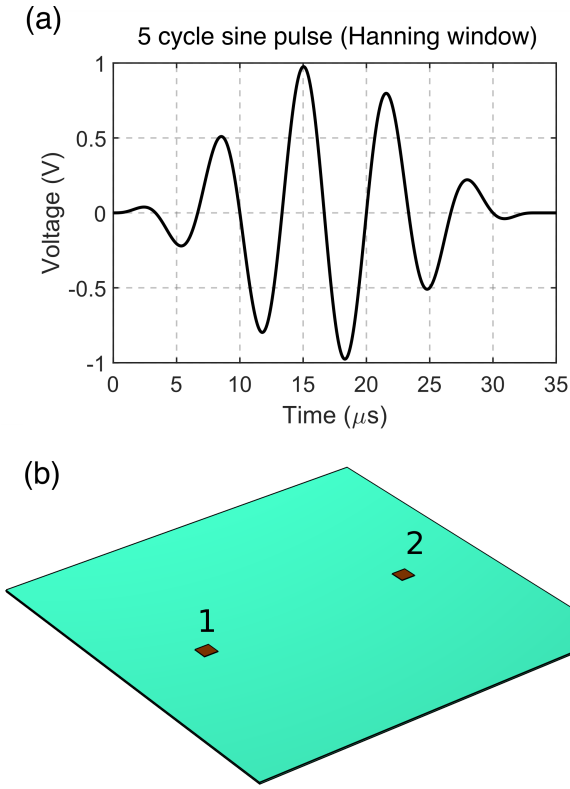


FIG. 6. (a) Input signal to transmitter: 150 kHz five-cycle sine pulse shaped by a Hanning window. (b) Setup for studying impact of temperature on group velocity of GW modes: 530 mm \times 530 mm \times 2 mm Al 6061-T6 plate with 20 mm \times 20 mm PZT transmitter (1) and receiver (2) spaced apart by 300 mm distance.

quired for performing simulations, the following method was used to generate datasets at various temperatures. Group velocities for the symmetric and anti-symmetric modes were obtained from analytical solutions of equations (9) and (10), using the expression in equation (15). FE simulations were performed for healthy (damage-free) and various damage conditions at 0 °C temperature. The temperature-dependent elastic properties (Figure 4) were used to determine group velocities of S_0 & A_0 modes for temperatures ranging from 0 °C to 100 °C. Generally, both S_0 and A_0 modes are commonly used for damage detection in isotropic plates [46]. However, S_0 mode is faster and has much lower attenuation than A_0 mode and therefore can propagate longer distances [46, 47]. In our present study, we focused on interaction of S_0 mode with the damage. For estimating the signal at temperature T , the GW signal obtained from FE simulation for 0 °C for any transmitter-receiver path on the panel was time-shifted by an amount Δt_T :

$$\Delta t_T = \frac{d}{c_{gT}} - \frac{d}{c_{g0}} \quad (17)$$

where d is the distance between the transmitter-receiver pair under consideration, c_{gT} is the analytically calcu-

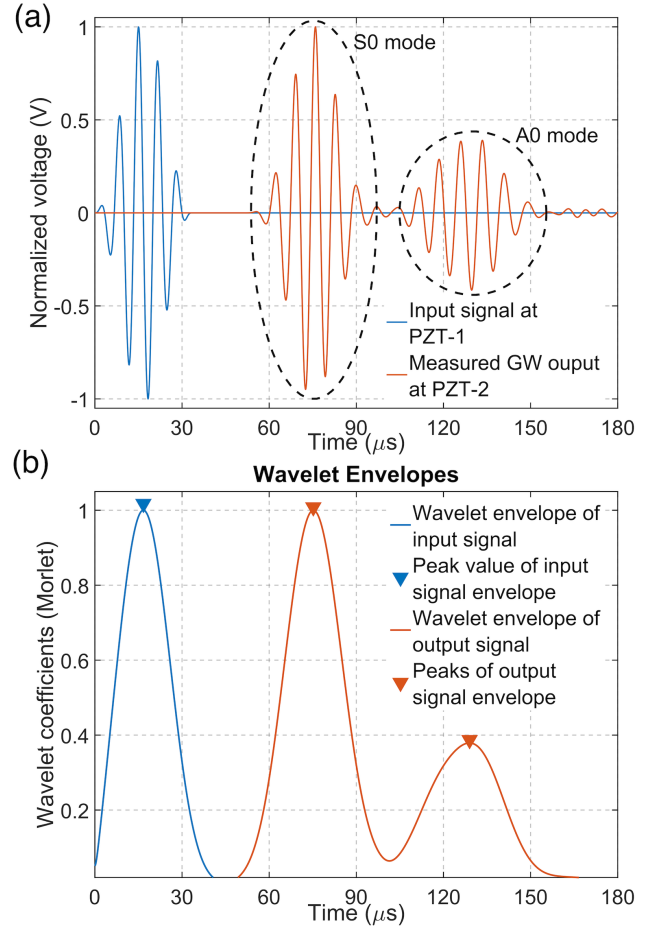


FIG. 7. (a) Input signal (blue trace) at transmitter (PZT-1) and GW signal recorded at receiver (PZT-2), showing S_0 and A_0 modes. (b) Time of flight for each mode is measured by the peak to peak distance of the wavelet envelopes of the corresponding signal at receiver from the time instant corresponding to peak value of input signal envelope.

lated group velocity of S_0 mode at temperature T , and c_{g0} is the analytically calculated group velocity of S_0 mode at 0 °C. The variation of signal amplitude with temperature was computed using the amplitude of S_0 wave packet for temperature ranging from 0 °C to 100 °C obtained analytically using *Dispersion calculator*, *DC* software [48]. The maximum amplitude value of S_0 wave packet was observed to vary linearly with increasing temperature. An analytical relation between A_f (ratio of maximum amplitude of S_0 wave packet at temperature T to that at 0 °C) and temperature T (specified in units of °C) ranging from 0 °C to 100 °C is obtained using MATLAB *Curve Fitting Toolbox*:

$$A_f = 1 + \frac{T \text{ [}^\circ\text{C]}}{3550} \quad (18)$$

The GW signal $s_T(t)$ at temperature T can thus be ob-

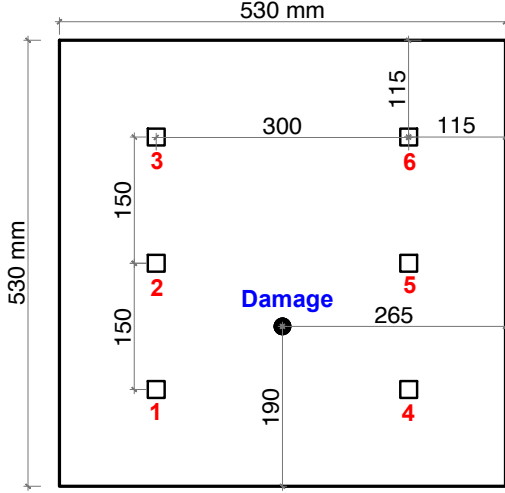


FIG. 8. Layout of Al 6061-T6 plate with network of six PZT transducers used for FE simulations. Three types of damages are considered (listed in Table II).

tained:

$$s_T(t) = A_f s_0(t + \Delta t_T) \quad (19)$$

where $s_0(t)$ is the signal at 0°C . This technique helps in reducing the computational time required for obtaining GW signals for all sensor paths at various temperatures, as this only requires time-consuming FE simulations at 0°C temperature. The data obtained at 0°C was used to generate data at other temperatures obtained using equation (19). To verify the accuracy of this method, we evaluated the cross-correlation coefficient between the signal obtained using equation (19) and that obtained from FE simulations performed at 50°C and 100°C . The cross-correlation coefficient was observed to be $>99\%$, and hence this method is justified to reduce computational complexity. Representative temperature-adjusted time-series for path P15 at two different temperatures: 0°C and 100°C , are shown in Figure 9(a). To incorporate uncertainties caused by variation in other EOCs and experimental uncertainties, we also added white noise and pink noise to the data:

$$s_{n,T}(t) = s_T(t) + \beta \max(s_T(t)) [w(t) + p(t)] \quad (20)$$

where $s_{n,T}(t)$ is the signal at temperature T with added noise, $\max(s_T(t))$ is the peak amplitude of signal $s_T(t)$, β is the noise scaling factor, and $w(n), p(n)$ are white noise and pink noise respectively, generated using normal distribution with zero mean and standard deviation of 0.1. We studied the performance of the damage assessment method for three different signal-to-noise-ratio (SNR) values: 2 dB, 4.5 dB and 10 dB. Figure 9(b) shows signal with added noise for $SNR = 2$ dB for sensor path P15 at 0°C .

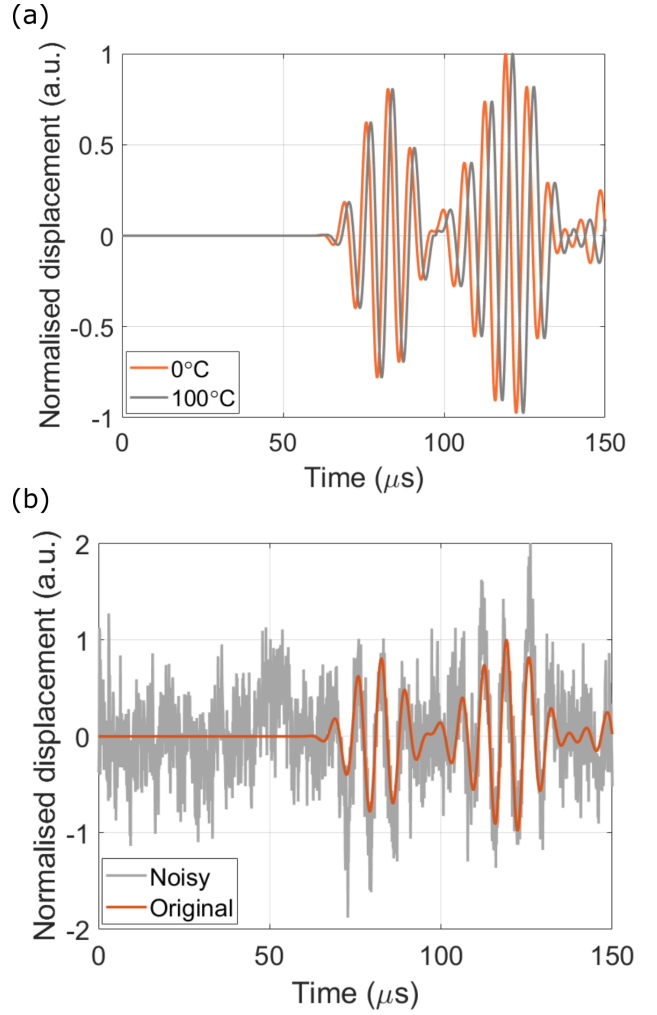


FIG. 9. (a) Effect of temperature on baseline GW data corresponding to sensor path P15. (b) Signal with added white noise and pink noise with 4.5 dB SNR, illustrated for sensor path P15 at 0°C .

IV. SIMULATION RESULTS AND DISCUSSION

To demonstrate and study the performance of the temperature compensated damage localization technique, the implementation was carried out in two phases: training phase and monitoring phase, as shown in Figure 10. The training phase involves data generation and training the CNNs (one CNN per path). The temperature affected GW data set with added noise described in the previous section was used for this purpose. The CNNs were trained using data corresponding to healthy i.e. undamaged (baseline) condition, as well as damaged conditions (rivet hole, added mass and notch). The penultimate layer of the trained CNN was then imported as feature extractor. Using the feature extractor, features for baseline data were computed and used for creating baseline GMM. These two modules, feature extractor and baseline GMM were imported as-is in the next phase i.e. moni-

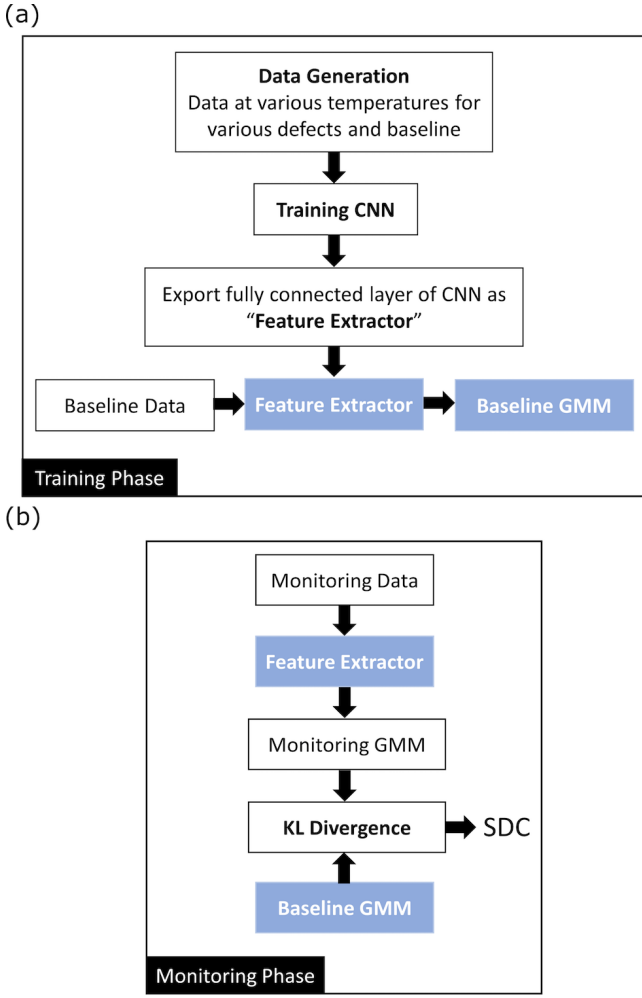


FIG. 10. Illustration of steps involved in training and monitoring phases. (a) The training phase involves data generation for training CNNs. It also involves modeling the baseline GMM. (b) Monitoring phase involves feature extraction from monitoring data. The feature extractor and baseline GMM are imported from training phase for computing SDC.

toring phase. The monitoring phase was designed such that it is readily deployable for real-time SHM. In this phase, GW data is collected from the structure being monitored. Using the feature extractor imported from training phase, features were computed for monitoring data which were then used to form monitoring GMM. Finally, the KL divergence between baseline GMM and monitoring GMM was computed. The values of KL divergence computed for each path are used as SDC for damage localization algorithm.

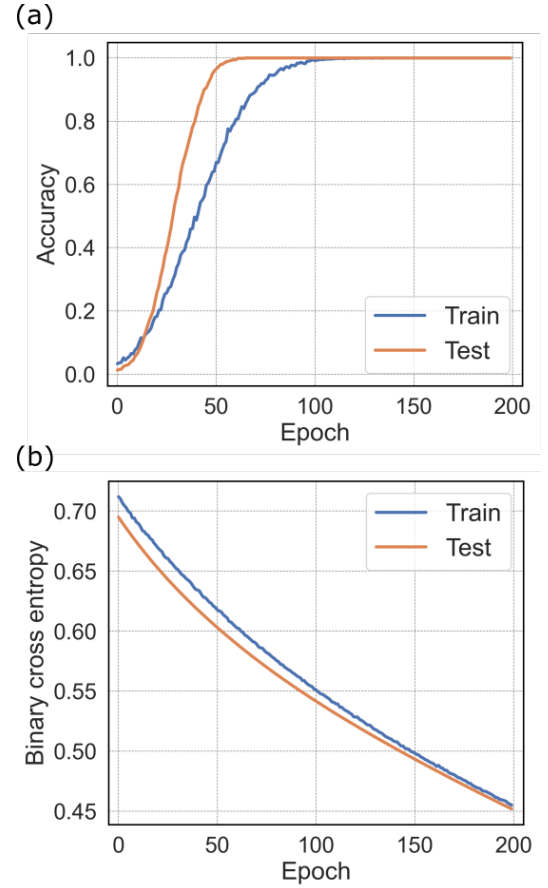


FIG. 11. (a) Accuracy, and (b) loss curves for training and testing of 1D CNN corresponding to sensor path P15 for 200 epochs.

A. Performance analysis of CNN+GMM based method for temperature compensated damage localization

The time-series dataset constructed using method summarised in equation (20) contained $200 \times 11 \times 4 \times 3 = 26\,400$ time-series for each path (200 series generated for each of the 11 different temperature values: 0°C , 10°C , $20^\circ\text{C} \dots 100^\circ\text{C}$, for each of the 4 classes: baseline, rivet hole, added mass, notch) and 3 different SNR values: 2 dB, 4.5 dB and 10 dB). Out of these 26 400 time-series, 13 200 were used for training the CNNs and the remaining series were divided into 10 sets that were used for performance analysis in monitoring phase. The training dataset (4400 series for each SNR for each path) was split in the proportion 75 : 20 : 5 (%) resulting in 3300 for training, 88 for testing, and 220 for validation of the CNNs. Each class was associated with a label generated with one-hot encoding, as listed in Table II. For each 1D CNN, learning rate of 1×10^{-7} and batch size of 64 were used. Binary cross-entropy loss was used as the cost function and Adam optimization scheme was used to enable momentum and adaptive learning rate in the training

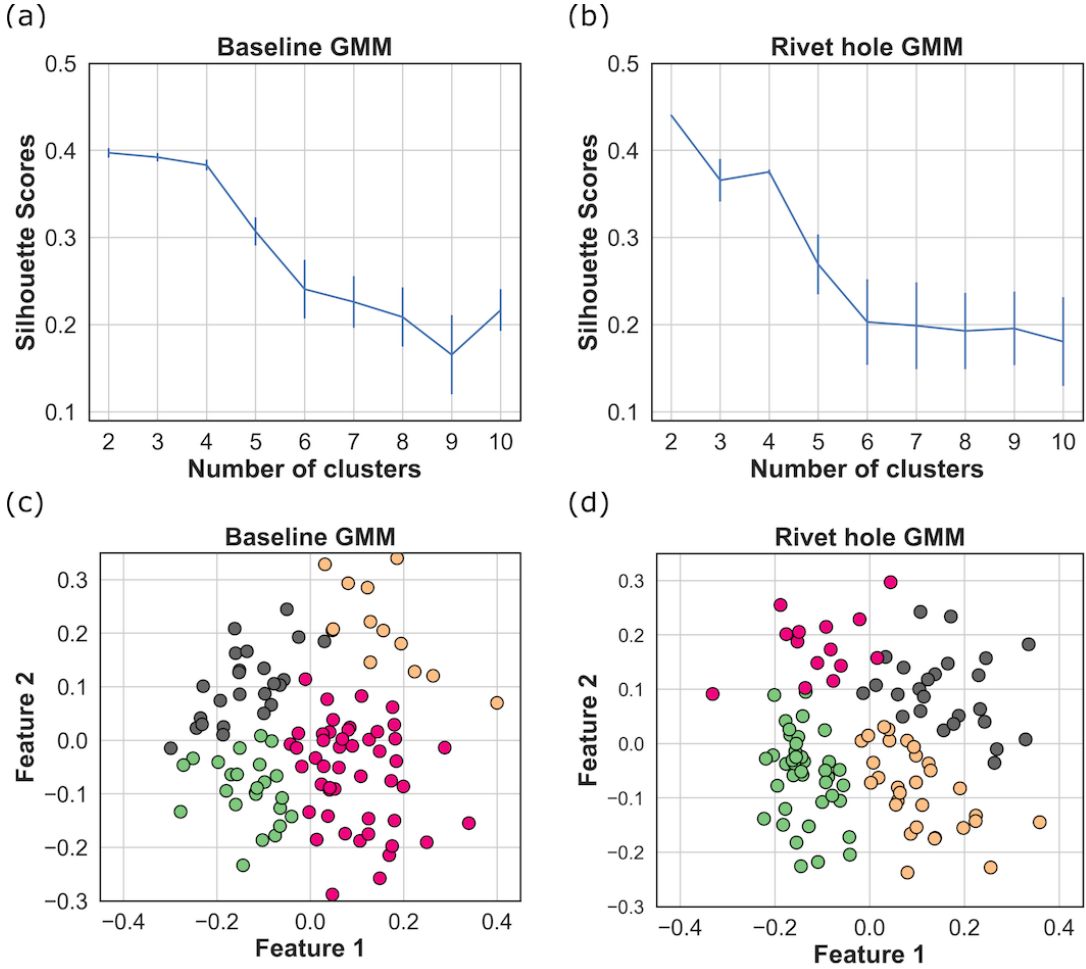


FIG. 12. For GMM-based clustering, optimum number of clusters are selected using silhouette score. Silhouette scores for various number of clusters for path P15 are shown for (a) baseline data, and (b) rivet hole data. Distributions formed using optimum number of clusters (4) are shown for two prominent features for (c) baseline data, and (d) rivet hole data. The two most prominent features were determined out of 16 features computed by the feature extractor layer in the CNN using PCA.

TABLE III. Summary of CNN architecture for binary classification of FE generated temperature and noise affected data

Layer (type)	Output shape	Number of parameters
Conv1D	1499×16	64
MaxPooling1D	749×16	0
Dropout	749×16	0
Flatten	11984	0
Dense (ReLU)	16	191760
Dense (Sigmoid)	4	68
Total trainable parameters		191892

process. The networks were trained for 200 epochs. The CNNs were trained on a 64-bit Intel® Core™-i7-10750H 2.60 GHz CPU workstation with 16 GB RAM. The models were developed in Python using TensorFlow library and Keras environment. The architecture of each 1D CNN is shown in Table III.

Representative accuracy and loss curves (for 200 epochs for path P15) are shown in Figure 11. The training loss as well as testing loss decrease smoothly with increasing number of epochs, thus indicating that the model is not over-fitting to the data. For over-fit models, the training error is extremely low while testing error increases sharply as the model tries to over-fit to noise present in the training samples. Perfect classification accuracy ($= 1$) was observed, which is not surprising for a homogeneous material such as aluminum. The penultimate layer of the CNN, used as feature extractor, yields 16 features for each time-series consisting of 1500 samples. These features were then processed by GMMs. Firstly, a baseline GMM for each path was created using features for 110 time-series chosen at random across the 11 different temperatures for each SNR. In monitoring phase, we evaluated the performance of the method using 10 different test cases using time-series data that were not used for training. Each of these 10 test cases also contained 110 time-series. Using the feature extrac-

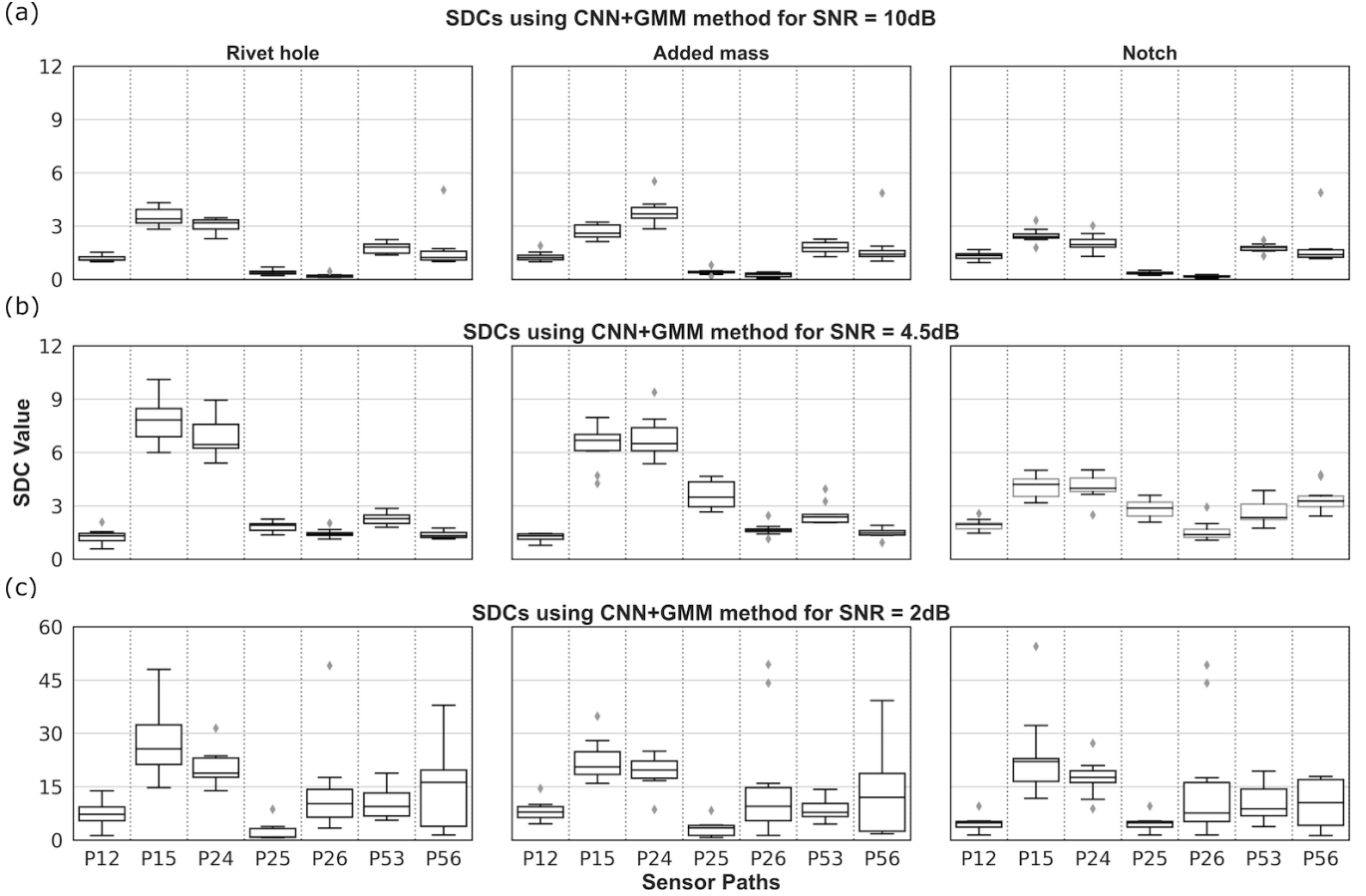


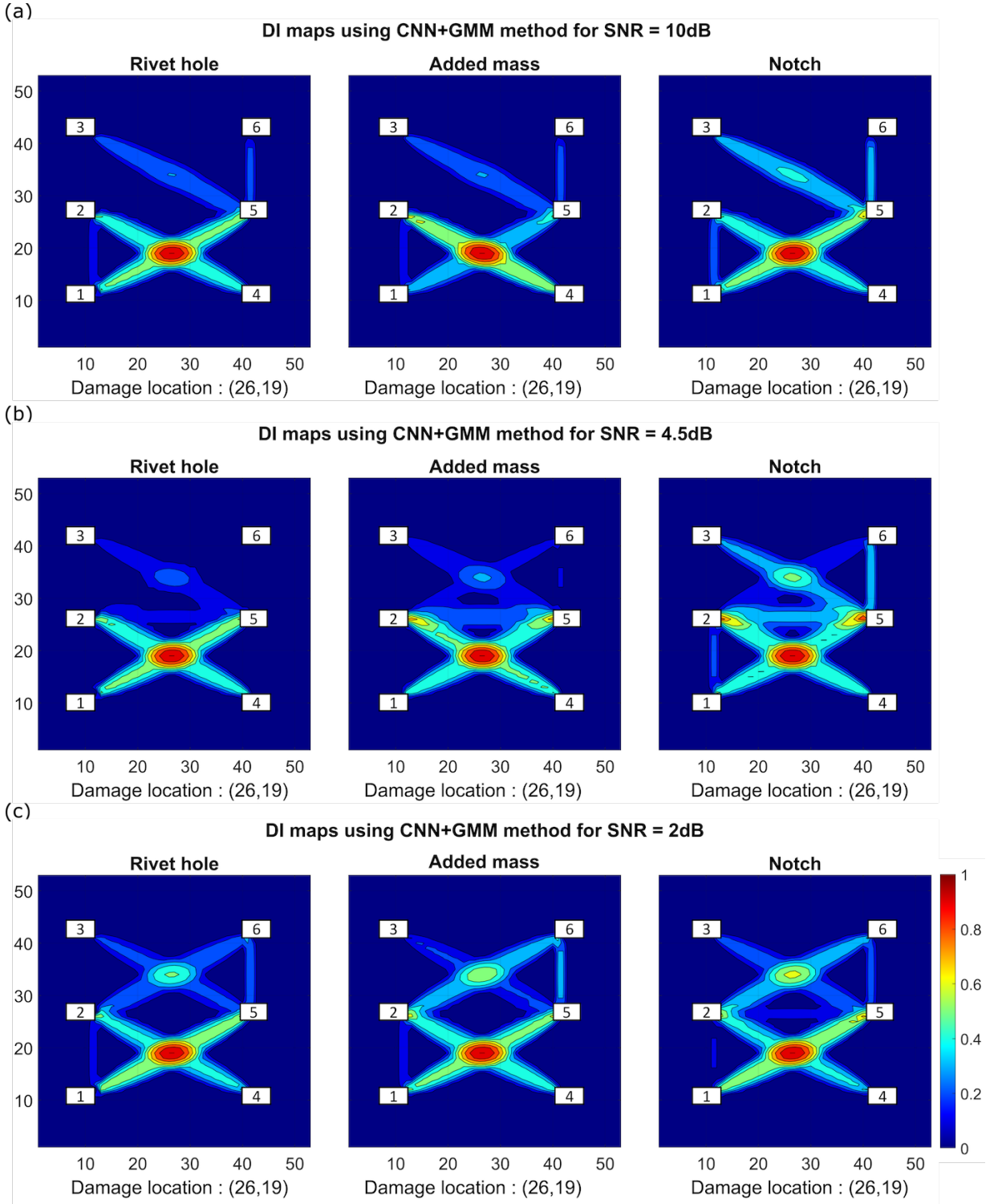
FIG. 13. Trends in SDCs computed using equation (5) as described in CNN+GMM method. For each of seven sensor paths, 10 values of SDCs are computed for 10 test cases. Three different defects are shown in 3 columns (rivet hole, added mass and notch). Three different signal to noise ratio (SNR) levels as shown in: (a) 10 dB, (b) 4.5 dB, and (c) 2 dB.

tor layer, we obtained feature set of size 16×110 that was used for creating monitoring GMM. To determine the optimum number of clusters in the GMM, silhouette score was computed by varying number of clusters for baseline features and monitoring (rivet hole) features as illustrated for path P15 in Figure 12(a) and (b), respectively. In both cases, the value of silhouette score dropped after beyond 4 clusters, therefore, for both GMMs, four clusters were formed as shown in in Figure 12(c) and (d). Next, KL divergence value was computed between baseline GMM and monitoring GMM using equation (5). The statistical distribution of values of KL-divergence i.e. SDC for 10 test cases and seven sensor paths are shown in Figure 13 for the three different SNR values. Both sensor paths containing the defect in-line (P15 and P24) show higher values of KL divergence compared to other five sensor paths which do not contain the defect. The corresponding DI maps are shown in Figure 14 for all SNR values. The DI maps are constructed using the mean value of SDC (from 10 test cases) for each path. The distinction between SDC values for paths containing the damage (P15 and P24) and paths without damage is better observed for higher SNRs, however the DI maps

accurately highlight the location of the damage even for $SNR = 2$ dB. Note that 2 dB SNR is unusually low in conventional GW SHM systems, however the proposed method is effective even with such low SNR. We observe that the distinction in SDC values for damaged and undamaged paths was more apparent for rivet hole and added mass, as compared to notch defect. This was attributed to the edge reflections in undamaged paths caused by the notch (dimension $60 \text{ mm} \times 7 \text{ mm}$). As shown in Figure 15, FE simulated GW signals for path P56 (that does not contain the damage) corresponding to baseline, rivet hole and added mass are very similar to each other (overlapping curves), whereas significant phase shift was observed for notch.

B. Comparison of CNN+GMM method vs. GMM using physics-defined features

To evaluate the efficacy of the CNN+GMM method, we compared the performance reported above to the method proposed by Ren et al. [31], that uses 2 features



(DI_1 and DI_2) and GMM for EOC compensation:

$$DI_1 = 1 - \sqrt{\frac{\{\int_{t_0}^{t_1} S_b(t)S_m(t)dt\}^2}{\{\int_{t_0}^{t_1} S_b(t)^2 dt \int_{t_0}^{t_1} S_m(t)^2 dt\}}} \quad (21)$$

$$DI_2 = \sqrt{\frac{\int_{f_0}^{f_1} \{|S_b(f)| - |S_m(f)|\}^2 df}{\int_{f_0}^{f_1} |S_b(f)|^2 df \int_{f_0}^{f_1} |S_m(f)|^2 df}} \quad (22)$$

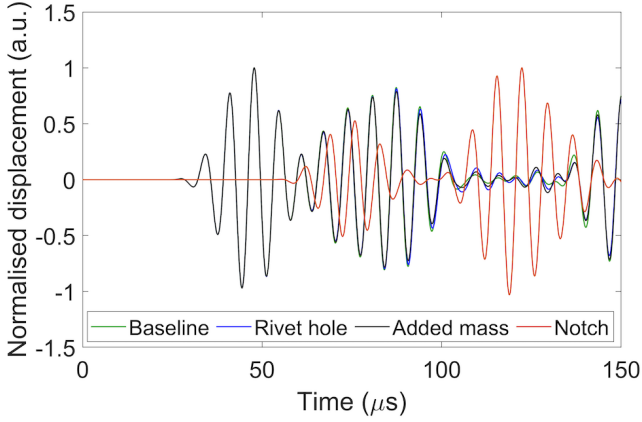


FIG. 15. GW signal corresponding to baseline, rivet hole, added mass and notch for sensor path P56 at 0°C. No significant difference from baseline is noticed for rivet hole and added mass cases. The signal obtained for notch damage shows significant difference as compared to the other signals.

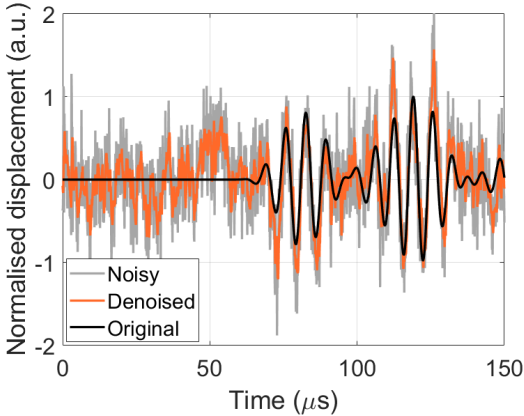


FIG. 16. Denoising of noisy signal using moving average filter with kernel size = 3 for GW signal corresponding to sensor path P15 at 0°C.

Feature DI_1 quantifies the correlation coefficient deviation between baseline signal $S_b(t)$ and monitoring signal $S_m(t)$, whereas feature DI_2 quantifies the difference in the Fourier spectra of baseline ($S_b(f)$) and monitoring ($S_m(f)$) signals, normalized to their respective energies. Here, t_0 is time of arrival for the S_0 mode and $t_1 = t_0 + t_w$ is the exit time, where $t_w = 33.3 \mu\text{s}$ is pulse width of actuation pulse (5-cycle sine wave with Hanning window in this case). Table IV lists the values of t_0 and t_1 for various sensor paths. The values of f_0 and f_1 were set to 100 kHz and 200 kHz respectively, given that the pulse actuation frequency is 150 kHz.

Using equations (21) and (22), we obtained feature vector of size 2×110 for each of the test case datasets. The same test case datasets reported above were used for this analysis. Using these features, we created two GMMs for each path (baseline and monitoring, for each damage) and computed their KL divergence. The trends in KL

TABLE IV. Time of arrival (t_0) and exit (t_1) of S_0 mode for various sensor paths.

Sensor Path	t_0 [μs]	t_1 [μs]
Vertical (P12, P56)	28	61.3
Horizontal (P25)	55.9	89.3
Diagonal (P15, P24, P26, P53)	62.5	95.9

divergence values for 10 test cases for $SNR = 4.5$ dB are illustrated in the top row in Figure 17. The distinction between damaged and undamaged paths is not as pronounced for the CNN+GMM method (Figure 13). Figure 18(a) shows that for rivet hole and added mass, the damage location was correctly identified in the DI map, whereas large error was observed for notch. Thus, using GMMs in conjunction with manually computed physics-defined features (DI_1 and DI_2) is not as effective as the CNN+GMM method for countering EOC variations.

C. Comparison of CNN+GMM method vs. conventional SDC algorithm using denoised signals

Conventional SDC computation algorithms work extremely well in well-controlled, laboratory environments where the noise levels are very low and uniform temperature is maintained. Since the CNN used in the CNN+GMM method involves filtering the input time-series signal, in this section we analyze the performance of conventional SDC computation algorithm on denoised input signals. The input signals with added noise and temperature variation (equation (20)) are denoised (i.e. filtered) using moving average kernel of size 3. The filtering operation is similar to the one performed by the CNN. Figure 16 illustrates a representative denoised time-domain signal for path P15. The denoised signals are then used for SDC computation using the conventional correlation coefficient deviation (CCD) definition [40]. Let S_d denote the signal received at receiver (j), and S_b denote the baseline signal. Let t_a denote the time of arrival for the desired GW mode in the signal and let t_{BW} denote the width of the time window corresponding to the wave mode (i.e. time bandwidth) of the desired GW mode. The SDC coefficient for sensor path $i - j$ is defined as measure of deviation of received signal S_d from baseline signal S_b and expressed as CCD:

$$SDC_{CCD}(i, j) = 1 - CC(i, j) \quad (23)$$

$$CC(i, j) = \frac{1}{\sigma_b \sigma_d} \frac{\sum_{t_a}^{t_a + t_{BW}} (S_b - \mu_b)(S_d - \mu_d)}{\sqrt{(\sum_{t_a}^{t_a + t_{BW}} (S_b - \mu_b)^2) (\sum_{t_a}^{t_a + t_{BW}} (S_d - \mu_d)^2)}} \quad (24)$$

Here, μ_b, μ_d are mean values and σ_b, σ_d are standard deviation values of the samples in baseline signal S_b and

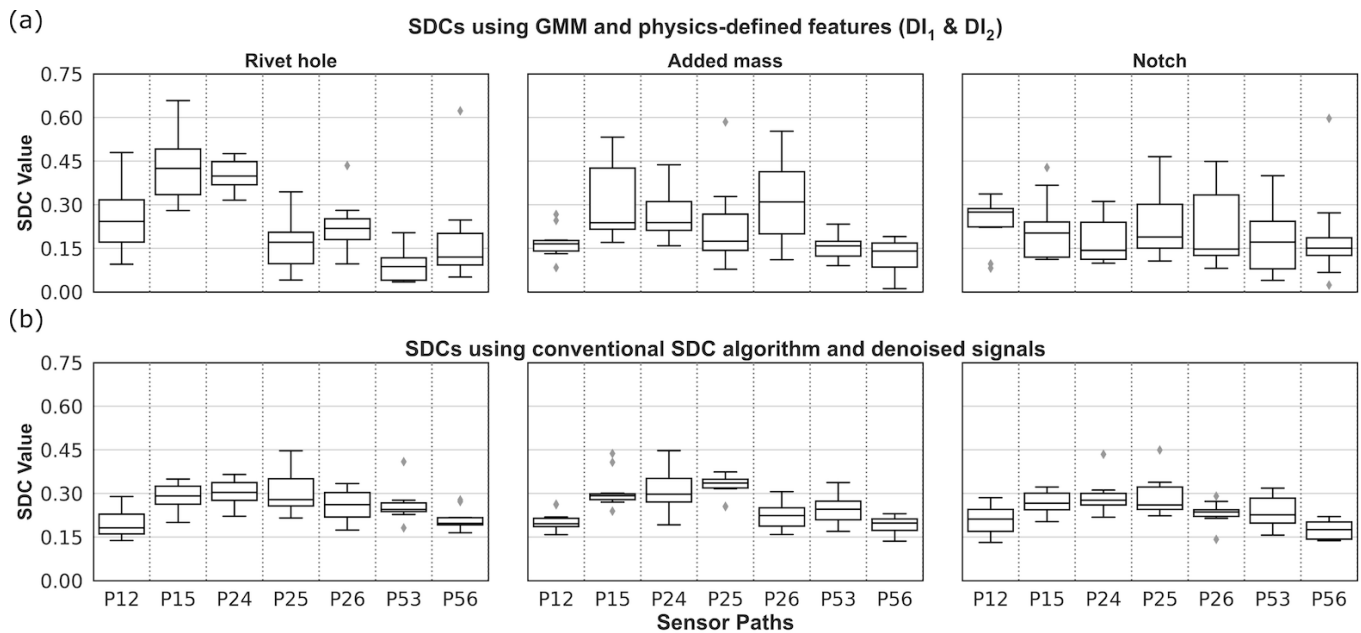


FIG. 17. Trends in SDCs computed using manually computed features. For each of seven sensor paths, 10 values of SDCs are computed for 10 test cases for SNR = 4.5 dB. Three different defects are shown in 3 columns (rivet hole, added mass and notch). SDCs are computed using (a) KL divergence of GMMs modeled using physics-defined features DI_1 and DI_2 (equations (21) and (22)), and (b) conventional SDC definition using CCD metric (equation (23)) applied to signals denoised using moving average kernel of size 3.

received signal S_d , respectively. The trends in SDC using equation (23) computed for the same 10 test cases for SNR = 4.5 dB are shown in the bottom row of Figure 17, and corresponding DI maps computed using the mean values of SDC_{CCD} are shown in Figure 18(b). This conventional method produces large errors and is thus entirely ineffective in countering EOC variations, thus validating the impact of the novel CNN+GMM method proposed in this work. It is important to note that the range of amplitudes of SDCs may vary depending on their definition (CCD, KL-divergence etc.) However, the relative difference in the values of SDCs for damaged paths and undamaged paths determines the accuracy of damage localization. Higher contrast between values of SDCs for damaged paths and undamaged paths yields better localization results. The DI maps are normalized to the pixel with the highest DI value i.e. the highest intensity in DI maps shown in Figures 14 and 18 is 1.

V. EXPERIMENTAL VALIDATION

A. Experimental setup

A portable embedded system was developed for transduction of guided wave ultrasonic signals and data acquisition and storage. The system is based on a low-cost field programmable gate array (FPGA) device (Xilinx Artix®-7 XC7A15T-1CPG236C, Digilent Cmod A7-15T module), and has provision for connecting 8 PZT

channels. The FPGA is interfaced with a 12 bit, parallel input, multiplying digital to analog converter (DAC) - Texas Instruments DAC7821, to generate the 5-cycle Hanning pulse actuation voltage centered at 150 kHz. Since the DAC7821 is an unbuffered current output DAC, a transimpedance amplifier constructed with Texas Instruments TL072 operational amplifier IC is connected to the output of the DAC, resulting in peak-to-peak amplitude of 4.8 V for the 5-cycle Hanning pulse. The receiver PZT output is amplified using Texas Instruments INA128 instrumentation amplifier and digitized using Maxim Integrated MAX-1426 analog to digital converter (ADC) with 10 bit resolution and 10 Msps sampling rate. The system is implemented on a printed circuit board (PCB), with the 8 channels connected to the ADC and DAC using 8-position switch banks. The system is capable of storing 4096 samples obtained at 10 Msps i.e. 409.6 μ s for each channel in the memory (Block RAM) in the FPGA. A photograph of the PCB is shown in Figure 19.

An aluminum panel of dimensions 530 mm \times 530 mm \times 2 mm was used as test structure in the experiment. Four PZT-5H transducers of dimensions 20 mm \times 20 mm \times 0.4 mm were attached on the panel with center-to-center separation of 90 mm in horizontal and vertical directions, as shown in the layout in Figure 20. Baseline data for all sensor paths were recorded at room temperature on the panel without any damage. Next, 8 data sets were collected by applying heat to a portion of the panel using a heat source (hair dryer), as shown in Figure 21(a). For each data set,

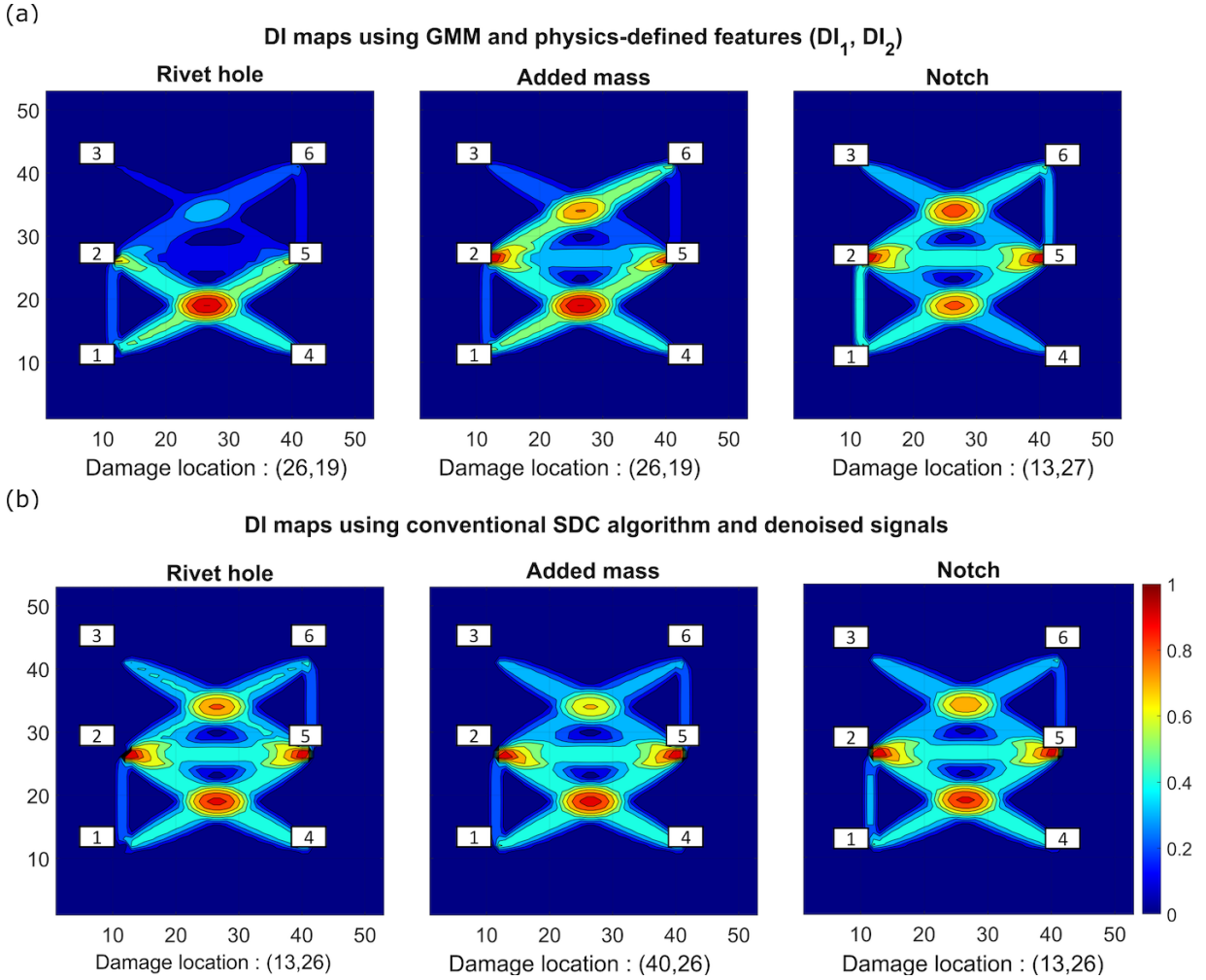


FIG. 18. DI maps obtained using SDC based damage localization algorithm. Mean value of SDCs across 10 test cases shown in Figure 17 was used to represent SDC of each sensor path. Three different defects are shown in 3 columns (rivet hole, added mass and notch). SDCs are computed using (a) KL divergence of GMMs modeled using physics-defined features DI_1 and DI_2 (equations (21) and (22)), and (b) conventional SDC definition using CCD metric (equation (23)) applied to signals denoised using moving average kernel of size 3.

the heat source was held atop an arbitrarily chosen location on the panel for up to 2 minutes, after which the heat source was removed and the data for all paths were recorded sequentially (Figure 21(b) shows indicative data for path P34 corresponding to heat source position in Figure 21(a)). Next, a notch defect of dimensions $10\text{ mm} \times 3\text{ mm}$ was introduced in the panel using a handheld electric drill (position shown in Figure 20, photograph of defect shown in Figure 21(c)). After introduction of the notch defect, 9 data sets were collected - one at room temperature, and 8 data sets for various non-uniform temperature profiles using the heat source. Figure 22 shows indicative photographs of the panel obtained with FLIR E60 thermal imaging camera during and after application of heat.

B. Experimental results and discussion

Data for four sensor paths (P12, P13, P14, P24, for sensor positions as marked in Figure 20) was considered for analysis. The data thus recorded were denoised using 5^{th} and 6^{th} coefficients of 7-level wavelet decomposition, using Daubechies 10 (db10) as mother wavelet. This is essential to remove electronic offset from the circuit components on the PCB. Next, each of the 9 data sets collected for undamaged panel and panel with notch defect was used to generate noise-augmented data with 4.5 dB SNR (in a manner similar to equation (20)). For each class (undamaged and notch), a total of 900 noise-augmented time series were generated per path for training CNN for binary classification, and additional 90 time series per path were generated for testing (monitoring). Table V shows an overview of the CNN model used for analyzing the experimental data. The model was trained

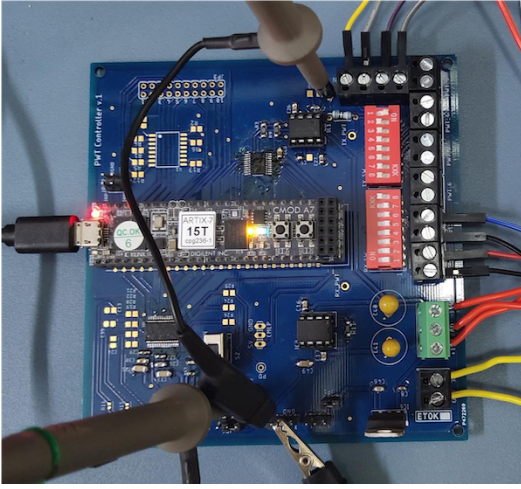


FIG. 19. Photograph of the PCB embedded platform for transduction and data acquisition used for performing experiments.

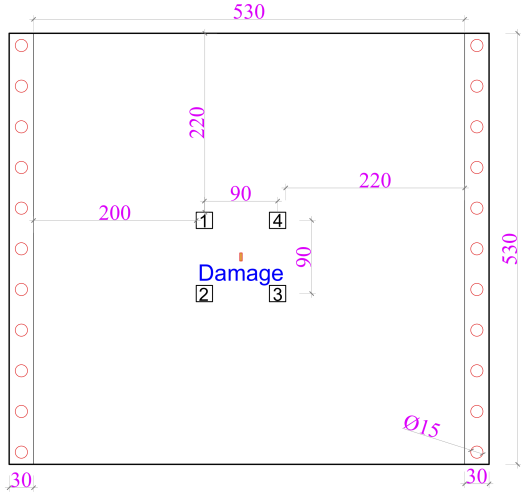


FIG. 20. Layout of 2 mm thick aluminum panel with 4 PZT transducers used for experimental testing. A notch defect of dimensions 10 mm \times 3 mm was introduced in the panel.

for 200 epochs, and produced perfect (100%) accuracy with test data sets. Since the sensors are placed closer to each other (90 mm separation along horizontal and vertical paths) on the panel used in the experiment, as compared to the FE generated data (150 mm and 300 mm separation between adjacent sensors along vertical and horizontal paths respectively), we use the first 100 μ s portion of each time series, that contain the S_0 mode. Accuracy curves (for 200 epochs for path P24) are shown in Figure 23.

Out of the 16 features extracted from the penultimate layer of the CNN, the 2 most prominent features (determined using PCA) were used to construct GMMs. The optimum number of clusters was determined to be 3, based on the silhouette score (Figure 24). KL divergence between the two GMMs was calculated as de-

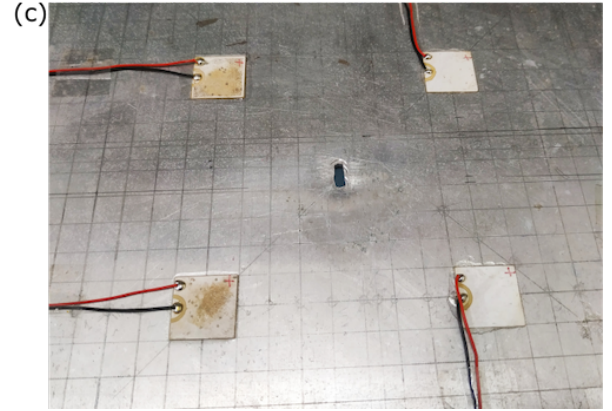
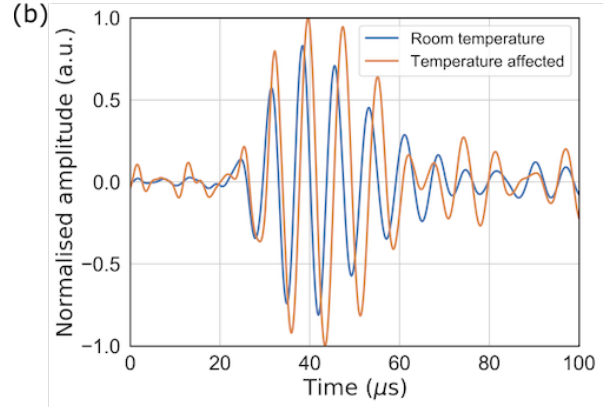
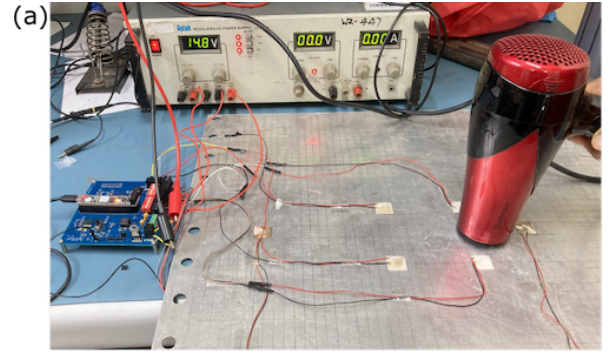


FIG. 21. (a) Photograph of aluminum panel (without damage) instrumented with PZT transducers connected to PCB. A hair dryer was used to heat a portion of the panel (example, above path P34 as shown) to induce non-uniform temperature profile on the panel. (b) Indicative temperature affected data for panel with notch defect at room temperature and in presence of non-uniform temperature variation for path P34. (c) Photograph of notch defect introduced in the panel.

scribed in equation (5). To illustrate the performance of CNN+GMM method for experimental data, comparative analysis was conducted using GMM with physics-defined features DI_1 and DI_2 as well as conventional SDC algorithm (CCD) with denoised signals as explained in subsections IV B and IV C, respectively. For 90 test samples, values of DI_1 and DI_2 were computed for baseline and notch data sets. The time of arrival and exit time for

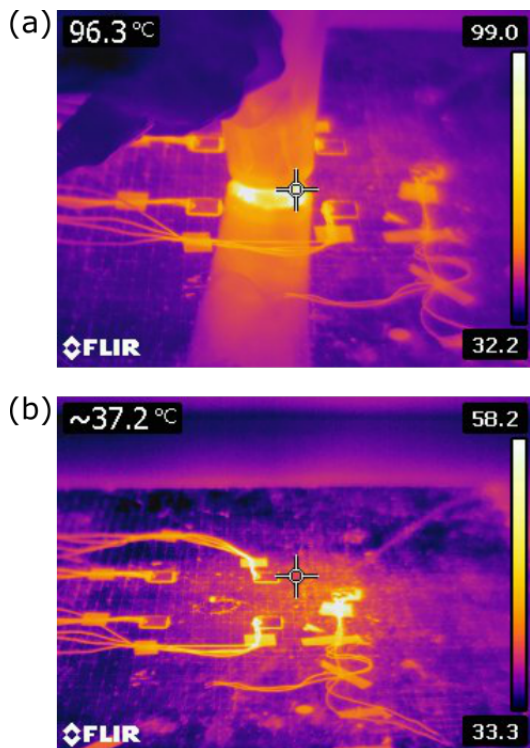


FIG. 22. Photographs of panel captured with thermal imaging camera. (a) Highest temperature reached during application of heat with hair dryer is approximately 100 °C. (b) Non-uniform heating of the panel is noticed in the image captured few seconds after removal of heat source. The heat source was present atop the location identified by the marker in the middle of the image.

TABLE V. Summary of CNN architecture for binary classification of experimental data

Layer (type)	Output shape	Number of parameters
Conv1D	997 × 16	64
MaxPooling1D	498 × 16	0
Dropout	498 × 16	0
Flatten	7968	0
Dense (ReLU)	16	127504
Dense (Sigmoid)	2	34
Total trainable parameters		127602

various sensor paths used for DI_1 and DI_2 computation are listed in Table VI. KL divergence between the two GMMs formed using the feature vector of size 90×2 for each sensor path was used for DI mapping. In case of conventional SDC algorithm using CCD, the average of CCD values of the 90 denoised test samples for each path was considered for the computation. SDC values for noise augmented test data using the three approaches are listed in Table VII and DI maps obtained using these SDC values are shown in Figure 25. We observe that only CNN+GMM method yields higher SDC values for paths containing the damage (diagonal paths) as compared to

TABLE VI. Time of arrival (t_0) and exit (t_1) of S_0 mode for various sensor paths in experimental data set.

Sensor Path	t_0 [μs]	t_1 [μs]
Vertical (P12)	16.8	50.1
Horizontal (P14)	16.8	50.1
Diagonal (P13, P24)	28	61.3

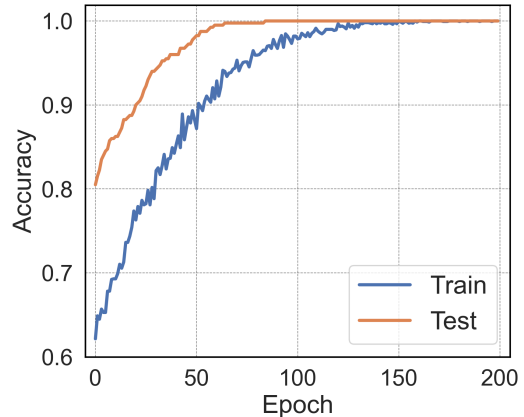


FIG. 23. Accuracy curves for training and testing of 1D CNN corresponding to sensor path P24 in noise-augmented experimental data set for 200 epochs.

other paths, and therefore gives correct damage location for temperature affected experimental data.

VI. CONCLUSION AND FUTURE WORK

The proof of concept implementation of the proposed method is illustrated for GW-SHM system consisting six-sensor network mounted atop an aluminum plate, with FE simulation based data generated at various temperatures from 0 °C to 100 °C, with added white noise and pink noise with SNR varied from 2 dB to 10 dB, and experimental data with non-uniform temperature variation and added noise. We have conclusively demonstrated that CNN-based automated feature computation and analysis using KL divergence of GMMs of features to represent SDC gives far superior performance as compared to conventional methods reported previously in literature, using both simulated as well as experimental data sets. Furthermore, the CNN-based approach requires no domain knowledge (wave velocity, impact of damage on amplitude and phase of wave modes etc.) and is therefore applicable broadly for various structures. To illustrate the efficacy of the method for damage classification and localization, the proposed algorithm was tested for different types of defects (rivet hole, added mass and notch), albeit with the same defect location, at the intersection of two diagonal sensor paths in the network. The experimental validation with notch defect also required the damage location to be at the intersection of the diag-

TABLE VII. Comparison of SDC values computed using various methods for noise-augmented experimental data. Only the CNN+GMM method shows higher SDC values for paths containing damage (diagonal paths) as compared to the vertical and horizontal paths. Numbers in parentheses indicate normalized value of SDC for each method.

Sensor path	Proposed method	CNN+GMM	GMM and physics defined features (DI_1 and DI_2)	Conventional SDC algorithm (CCD) and denoised signal
P12 (Vertical)	0.02 (0.05)		6.62 (0.73)	0.64 (1)
P14 (Horizontal)	0.05 (0.12)		1.54 (0.17)	0.41 (0.64)
P13 (Diagonal)	0.41 (1)		1.44 (0.16)	0.24 (0.38)
P24 (Diagonal)	0.17 (0.41)		9.11 (1)	0.39 (0.61)

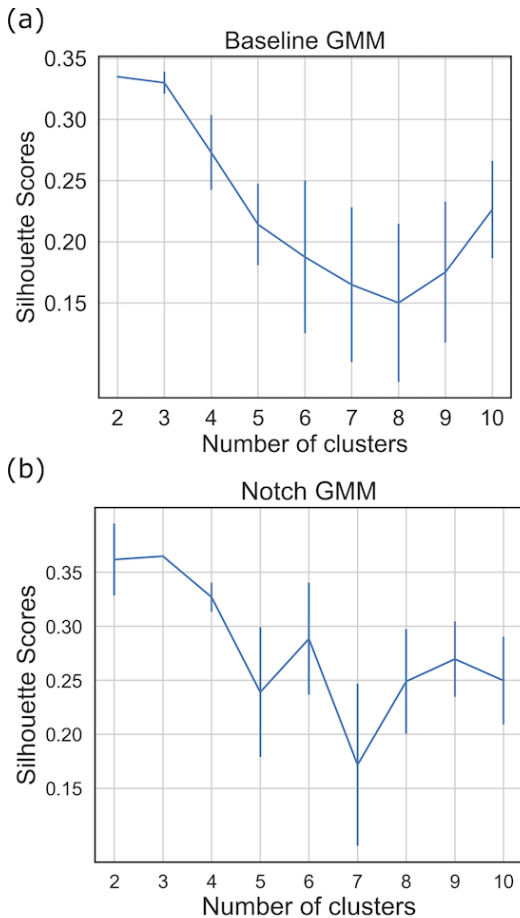


FIG. 24. Silhouette scores for various number of clusters for path P24 in noise-augmented experimental data set, shown for (a) baseline (undamaged panel), and (b) notch defect.

onal paths. This constraint was necessary, since the SDC based damage localization algorithm used to compute DI maps has limited spatial resolution and requires a grid of

sensors. This method is most sensitive to damages that are present at the intersection of ellipses corresponding to different sensor paths. In future work, we will explore alternate methods to improve the spatial resolution of the damage localization using methods such as outer-tangent method [49] and delay and sum algorithm [50], and also by employing deep learning coupled with regression. Availability of extensive labeled data significantly limits the applicability of supervised learning algorithms. Therefore we also seek to explore unsupervised learning and transfer learning based approaches that have more applicability and warrant further research. Additionally, we seek to also explore development of light-weight deep learning models inspired by TinyML framework [51], that could be directly embedded in the FPGA based embedded system presented in this work, to truly design portable smart SHM systems.

ACKNOWLEDGMENT

This work was partially supported by Indian Space Research Organization (ISRO) [grant no. RD/0118-ISROC00-006]. The authors thank Ms. Sahar Almahfouz Nasser and Prof. Amit Sethi at IIT Bombay for insightful discussions on deep learning, and Mr. Rambabu Sugguna at National Centre for Photovoltaic Research and Education (NCPRE), IIT Bombay for assistance with thermal imaging.

DECLARATION OF INTERESTS

The authors declare that they have no known competing financial interests or personal relationships that could have appeared to influence the work reported in this paper.

[1] M. Mitra and S. Gopalakrishnan, Guided wave based structural health monitoring: A review, *Smart Materials and Structures* **25**, 053001 (2016).

[2] F. Yan, R. L. Royer Jr, and J. L. Rose, Ultrasonic guided wave imaging techniques in structural health monitoring, *Journal of intelligent material Systems and Structures* **21**, 377 (2010).

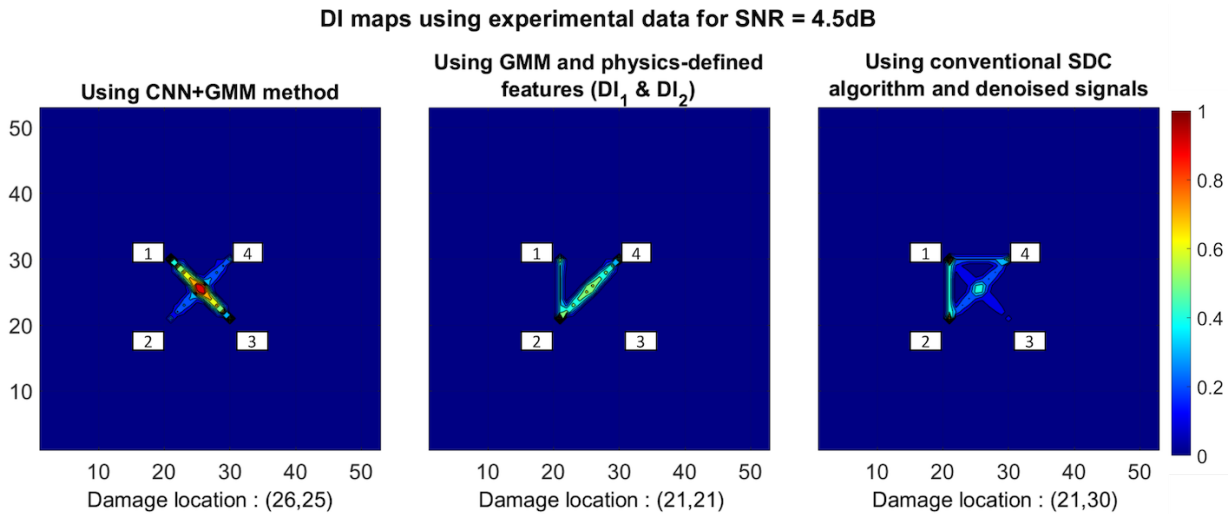


FIG. 25. DI maps for noise-augmented experimental data under varying non-uniform temperature profiles on aluminum panel with notch defect, obtained using SDC based damage localization algorithm. SDCs are computed using computed using: (a) the proposed CNN+GMM method as described in equation 5, (b) KL divergence of GMMs modeled using physics-defined features DI_1 and DI_2 (equations (21) and (22)), and (c) conventional SDC definition using CCD metric (equation (23)) applied to signals denoised using moving average kernel of size 3. Only the proposed CNN+GMM method is able to accurately localize the damage on the panel.

- [3] M. Abbas and M. Shafiee, Structural health monitoring (SHM) and determination of surface defects in large metallic structures using ultrasonic guided waves, *Sensors* **18**, 3958 (2018).
- [4] V. A. Attarian, F. B. Cegla, and P. Cawley, Long-term stability of guided wave structural health monitoring using distributed adhesively bonded piezoelectric transducers, *Structural health monitoring* **13**, 265 (2014).
- [5] P. Cawley, Structural health monitoring: Closing the gap between research and industrial deployment, *Structural Health Monitoring* **17**, 1225 (2018).
- [6] G. Konstantinidis, B. W. Drinkwater, and P. D. Wilcox, The temperature stability of guided wave structural health monitoring systems, *Smart Materials and Structures* **15**, 967 (2006).
- [7] T. Clarke, P. Cawley, P. D. Wilcox, and A. J. Croxford, Evaluation of the damage detection capability of a sparse-array guided-wave SHM system applied to a complex structure under varying thermal conditions, *IEEE transactions on ultrasonics, ferroelectrics, and frequency control* **56**, 2666 (2009).
- [8] K. J. Schubert and A. S. Herrmann, On the influence of moisture absorption on Lamb wave propagation and measurements in viscoelastic CFRP using surface applied piezoelectric sensors, *Composite Structures* **94**, 3635 (2012).
- [9] A. C. Douglass and J. B. Harley, Model-based statistical guided wave damage detection for an aluminum plate, *Structural Health Monitoring* **19**, 1937 (2020).
- [10] S. Roy, P. Ladpli, and F.-K. Chang, Load monitoring and compensation strategies for guided-waves based structural health monitoring using piezoelectric transducers, *Journal of Sound and Vibration* **351**, 206 (2015).
- [11] S. Sikdar, P. Fiborek, P. Kudela, S. Banerjee, and W. Ostachowicz, Effects of debonding on Lamb wave propagation in a bonded composite structure under variable temperature conditions, *Smart Materials and Structures* **28**, 015021 (2018).
- [12] A. J. Croxford, J. Moll, P. D. Wilcox, and J. E. Michaels, Efficient temperature compensation strategies for guided wave structural health monitoring, *Ultrasonics* **50**, 517 (2010).
- [13] H. Sohn, Effects of environmental and operational variability on structural health monitoring, *Philosophical Transactions of the Royal Society A: Mathematical, Physical and Engineering Sciences* **365**, 539 (2007).
- [14] K. Zolna, P. B. Dao, W. J. Staszewski, and T. Barszcz, Towards homoscedastic nonlinear cointegration for structural health monitoring, *Mechanical Systems and Signal Processing* **75**, 94 (2016).
- [15] A. H. Seno, Z. S. Khodaei, and M. F. Aliabadi, Passive sensing method for impact localisation in composite plates under simulated environmental and operational conditions, *Mechanical Systems and Signal Processing* **129**, 20 (2019).
- [16] M. Mousavi and A. H. Gandomi, Prediction error of Johansen cointegration residuals for structural health monitoring, *Mechanical Systems and Signal Processing* **160**, 107847 (2021).
- [17] P. B. Dao and W. J. Staszewski, Lamb wave based structural damage detection using cointegration and fractal signal processing, *Mechanical Systems and Signal Processing* **49**, 285 (2014).
- [18] E. S. Tomé, M. Pimentel, and J. Figueiras, Damage detection under environmental and operational effects using cointegration analysis—Application to experimental data from a cable-stayed bridge, *Mechanical Systems and Signal Processing* **135**, 106386 (2020).
- [19] C. Liu, J. B. Harley, M. Bergés, D. W. Greve, and I. J. Oppenheim, Robust ultrasonic damage detection under complex environmental conditions using singular value decomposition, *Ultrasonics* **58**, 75 (2015).

- [20] T. Clarke, F. Simonetti, and P. Cawley, Guided wave health monitoring of complex structures by sparse array systems: Influence of temperature changes on performance, *Journal of Sound and Vibration* **329**, 2306 (2010).
- [21] J. Dobson and P. Cawley, Independent component analysis for improved defect detection in guided wave monitoring, *Proceedings of the IEEE* **104**, 1620 (2015).
- [22] R. Gorgin, Y. Luo, and Z. Wu, Environmental and operational conditions effects on Lamb wave based structural health monitoring systems: A review, *Ultrasonics* **105**, 106114 (2020).
- [23] O. Abdeljaber, O. Avci, S. Kiranyaz, M. Gabbouj, and D. J. Inman, Real-time vibration-based structural damage detection using one-dimensional convolutional neural networks, *Journal of Sound and Vibration* **388**, 154 (2017).
- [24] A. Khan, D.-K. Ko, S. C. Lim, and H. S. Kim, Structural vibration-based classification and prediction of delamination in smart composite laminates using deep learning neural network, *Composites Part B: Engineering* **161**, 586 (2019).
- [25] Y. Bao, Z. Tang, H. Li, and Y. Zhang, Computer vision and deep learning-based data anomaly detection method for structural health monitoring, *Structural Health Monitoring* **18**, 401 (2019).
- [26] A. Aria, E. L. Drogue, S. Azarm, and M. Modarres, Estimating damage size and remaining useful life in degraded structures using deep learning-based multi-source data fusion, *Structural Health Monitoring* **19**, 1542 (2020).
- [27] I. N. Giannakeas, Z. S. Khodaei, and M. Aliabadi, Digital clone testing platform for the assessment of SHM systems under uncertainty, *Mechanical Systems and Signal Processing* **163**, 108150 (2022).
- [28] L. Xu, S. Yuan, J. Chen, and Y. Ren, Guided wave-convolutional neural network based fatigue crack diagnosis of aircraft structures, *Sensors* **19**, 10.3390/s19163567 (2019).
- [29] P. Pandey, A. Rai, and M. Mitra, Explainable 1-D convolutional neural network for damage detection using Lamb wave, *Mechanical Systems and Signal Processing* **164**, 108220 (2022).
- [30] M. Rautela and S. Gopalakrishnan, Ultrasonic guided wave based structural damage detection and localization using model assisted convolutional and recurrent neural networks, *Expert Systems with Applications* , 114189 (2020).
- [31] Y. Ren, L. Qiu, S. Yuan, and F. Fang, Gaussian mixture model-based path-synthesis accumulation imaging of guided wave for damage monitoring of aircraft composite structures under temperature variation, *Structural Health Monitoring* **18**, 284 (2019).
- [32] Y. Ren, L. Qiu, S. Yuan, and F. Fang, Multi-damage imaging of composite structures under environmental and operational conditions using guided wave and Gaussian mixture model, *Smart Materials and Structures* **28**, 115017 (2019).
- [33] Y. Ren, L. Qiu, S. Yuan, and F. Fang, Gaussian mixture model and delay-and-sum based 4D imaging of damage in aircraft composite structures under time-varying conditions, *Mechanical Systems and Signal Processing* **135**, 106390 (2020).
- [34] H. Sun, J. Yi, Y. Xu, Y. Wang, and X. Qing, Identification and compensation technique of non-uniform temperature field for Lamb wave-and multiple sensors-based damage detection, *Sensors* **19**, 2930 (2019).
- [35] Y. Wang, G. Wang, D. Wu, Y. Wang, B. Miao, H. Sun, and X. Qing, An improved matching pursuit-based temperature and load compensation method for ultrasonic guided wave signals, *IEEE Access* **8**, 67530 (2020).
- [36] I. D. Khurjekar and J. B. Harley, Uncertainty aware deep neural network for multistatic localization with application to ultrasonic structural health monitoring, *arXiv preprint arXiv:2007.06814* (2020).
- [37] H. Liu and Y. Zhang, Deep learning based crack damage detection technique for thin plate structures using guided lamb wave signals, *Smart Materials and Structures* **29**, 015032 (2019).
- [38] J. Melville, K. S. Alguri, C. Deemer, and J. B. Harley, Structural damage detection using deep learning of ultrasonic guided waves, in *AIP Conference Proceedings*, Vol. 1949 (AIP Publishing LLC, 2018) p. 230004.
- [39] S. K. Pedram, S. Fateri, L. Gan, A. Haig, and K. Thornicroft, Split-spectrum processing technique for SNR enhancement of ultrasonic guided wave, *Ultrasonics* **83**, 48 (2018).
- [40] S. Sikdar and S. Banerjee, Identification of disbond and high density core region in a honeycomb composite sandwich structure using ultrasonic guided waves, *Composite Structures* **152**, 568 (2016).
- [41] D. A. Reynolds, Gaussian mixture models, *Encyclopedia of Biometrics* **741**, 659 (2009).
- [42] J. Goldberger, S. Gordon, H. Greenspan, *et al.*, An Efficient Image Similarity Measure Based on Approximations of KL-Divergence Between Two Gaussian Mixtures, in *ICCV*, Vol. 3 (2003) pp. 487–493.
- [43] J. Rose, *Ultrasonic Guided Waves in Solid Media* (2014) pp. 1–512.
- [44] C. A. Leckey, K. R. Wheeler, V. N. Hafiychuk, H. Hafiychuk, and D. A. Timuçin, Simulation of guided-wave ultrasound propagation in composite laminates: Benchmark comparisons of numerical codes and experiment, *Ultrasonics* **84**, 187 (2018).
- [45] Q. Lei, Y. Xixi, L. Xiaodong, and Y. Shenfang, Multiphysics simulation method of lamb wave propagation with piezoelectric transducers under load condition, *Chinese Journal of Aeronautics* **32**, 1071 (2019).
- [46] Z. Su, L. Ye, and Y. Lu, Guided lamb waves for identification of damage in composite structures: A review, *Journal of Sound and Vibration* **295**, 753 (2006).
- [47] N. P. Y. Faez A. Masurkar, Optimizing location of damage within an enclosed area defined by an algorithm based on the lamb wave response data, *Applied Acoustics* **120**, 98 (2017).
- [48] A. Huber, Dispersion Calculator (DC).
- [49] M. S. Hameed and Z. Li, Transverse damage localization and quantitative size estimation for composite laminates based on lamb waves, *IEEE Access* **7**, 174859 (2019).
- [50] J. E. Michaels and T. E. Michaels, Guided wave signal processing and image fusion for in situ damage localization in plates, *Wave Motion* **44**, 482 (2007), special Issue of Selected Papers Presented at the International Symposium on Mechanical Waves in Solids.
- [51] R. Sanchez-Iborra and A. F. Skarmeta, TinyML-enabled frugal smart objects: Challenges and opportunities, *IEEE Circuits and Systems Magazine* **20**, 4 (2020).